

# Physical mechanisms of transient enhanced dopant diffusion in ion-implanted silicon

P. A. Stolk,<sup>a)</sup> H.-J. Gossmann,<sup>b)</sup> D. J. Eaglesham, D. C. Jacobson, C. S. Rafferty, G. H. Gilmer, M. Jaraíz,<sup>c)</sup> and J. M. Poate  
*Bell Laboratories, Lucent Technologies, Murray Hill, New Jersey 07974*

H. S. Luftman  
*Bell Laboratories, Lucent Technologies, Breinigsville, Pennsylvania 18031*

T. E. Haynes  
*Oak Ridge National Laboratory, Oak Ridge, Tennessee 37831*

(Received 16 July 1996; accepted for publication 23 September 1996)

Implanted B and P dopants in Si exhibit transient enhanced diffusion (TED) during annealing which arises from the excess interstitials generated by the implant. In order to study the mechanisms of TED, transmission electron microscopy measurements of implantation damage were combined with B diffusion experiments using doping marker structures grown by molecular-beam epitaxy (MBE). Damage from nonamorphizing Si implants at doses ranging from  $5 \times 10^{12}$  to  $1 \times 10^{14}/\text{cm}^2$  evolves into a distribution of {311} interstitial agglomerates during the initial annealing stages at 670–815 °C. The excess interstitial concentration contained in these defects roughly equals the implanted ion dose, an observation that is corroborated by atomistic Monte Carlo simulations of implantation and annealing processes. The injection of interstitials from the damage region involves the dissolution of {311} defects during Ostwald ripening with an activation energy of  $3.8 \pm 0.2$  eV. The excess interstitials drive substitutional B into electrically inactive, metastable clusters of presumably two or three B atoms at concentrations below the solid solubility, thus explaining the generally observed immobile B peak during TED of ion-implanted B. Injected interstitials undergo retarded diffusion in the MBE-grown Si with an effective migration energy of  $\sim 3.5$  eV, which arises from trapping at substitutional C. The concept of trap-limited diffusion provides a stepping stone for understanding the enormous disparity among published values for the interstitial diffusivity in Si. The population of excess interstitials is strongly reduced by incorporating substitutional C in Si to levels of  $\sim 10^{19}/\text{cm}^3$  prior to ion implantation. This provides a promising method for suppressing TED, thus enabling shallow junction formation in future Si devices through dopant implantation. The present insights have been implemented into a process simulator, allowing for a significant improvement of the predictive modeling of TED. © 1997 American Institute of Physics. [S0021-8979(97)02101-4]

## I. INTRODUCTION

The advancing miniaturization of Si integrated circuits continues to expose severe gaps in our understanding of the role of defects and impurities in Si processing. A striking example is the phenomenon of transient enhanced diffusion (TED) which occurs when ion-implanted dopants in crystalline silicon (*c*-Si), such as B and P, are subjected to thermal annealing. The process of enhanced dopant diffusion was first recognized more than 20 years ago by Hofker *et al.*<sup>1</sup> The phenomenon has been extensively investigated in the past decade,<sup>2–8</sup> and its basic features have been well characterized.<sup>9–11</sup> As an illustration, Fig. 1 shows enhanced diffusion for a shallow B profile implanted into float-zone (FZ) crystalline silicon. Upon annealing at 800 °C for 35 min, B in the tail of the implanted profile has diffused over  $\sim 700$  Å, whereas the equilibrium diffusion length for these

annealing conditions is only  $\sim 25$  Å.<sup>12</sup> The nonequilibrium diffusion vanishes for longer annealing times,<sup>6,11</sup> which is the transient signature of TED. An additional feature of TED in Fig. 1 is that the peak portion of the B profile above  $10^{18}/\text{cm}^3$  is not electrically activated and has remained immobile during annealing. This is remarkable in view of the fact that the equilibrium solubility of B at 800 °C is higher than  $10^{19}/\text{cm}^3$ , suggesting that the entire B profile should be soluble and mobile.

It is by now well established that the anomalous diffusion of ion-implanted B and P arises from excess Si self-interstitials that are generated by the implant. The interstitials *I* couple with substitutional dopant atoms *A<sub>s</sub>* through the reaction



thereby forming a mobile dopant complex *A<sub>I</sub>*.<sup>12</sup> The increased interstitial concentration [*I*] in the ion-implanted region will shift the local equilibrium between substitutional and mobile dopant atoms, and the resulting enhanced dopant diffusivity  $D_A^{\text{enh}}$  is to good approximation given by<sup>12</sup>

<sup>a)</sup>Present address: Philips Research Laboratories, 5656 AA Eindhoven, The Netherlands. Electronic mail: stolk@natlab.research.philips.com

<sup>b)</sup>Electronic mail: hjg@bell-labs.com

<sup>c)</sup>Present address: Departamento de Electronica, Facultad de Ciencias, Universidad de Valladolid, 47011 Valladolid, Spain.

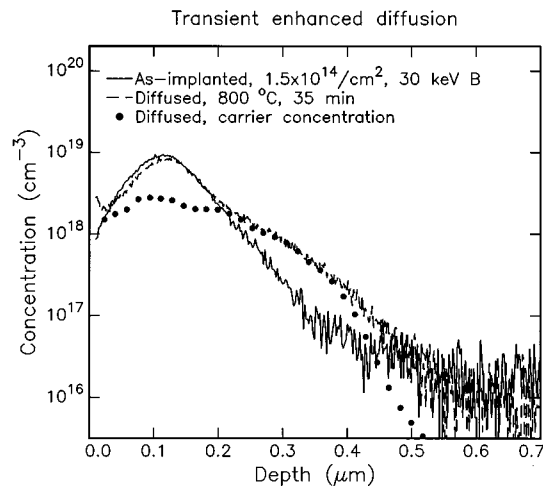


FIG. 1. Secondary-ion-mass spectrometry (lines) and spreading resistance (solid circles) measurements of an implanted B profile ( $1.5 \times 10^{14}/\text{cm}^2$ , 30 keV  $^{10}\text{B}$ ) before and after transient enhanced diffusion at 800 °C for 35 min.

$$D_A^{\text{enh}} = D_A^* \frac{[I]}{[I^*]}, \quad (2)$$

where  $D_A^*$  denotes the dopant diffusivity under equilibrium conditions and  $[I^*]$  the equilibrium interstitial concentration.

Although TED is minimal under rapid thermal annealing conditions (e.g., 1000 °C, 5 s),<sup>6</sup> it becomes more and more pronounced and critical with the continuing trend of reducing the thermal budget in device manufacturing. Hence, TED now threatens to impose severe limitations on the minimum device dimensions attainable in next generation devices. In addition, it has been shown that the lateral coupling between excess interstitials and dopants is responsible for the so-called reverse-short-channel effect,<sup>13,14</sup> which encumbers the scalability of metal-oxide-semiconductor (MOS) transistors. At present, simulation tools designed to predict dopant diffusion during device processing are not capable of dealing with TED in a satisfactory manner. From this perspective, it is crucial to improve our understanding of the physical mechanisms of TED. An additional scientific challenge is the development of processing-compatible methods for suppressing interstitial-enhanced dopant diffusion.

Among the uncertain factors which preclude accurate modeling of TED are the diffusion coefficient  $D_I$  and the equilibrium concentration  $[I^*]$  of the Si self-interstitial. As shown in a recent article by Bracht, Stolwijk, and Mehrer<sup>15</sup> studies on self-diffusion<sup>16</sup> and metal diffusion<sup>15,17</sup> in Si have yielded reasonably consistent values for the mass transport properties in Si, which implicitly contains the product  $D_I[I^*]$ . Separate determinations of  $D_I$  and  $[I^*]$ ,<sup>15</sup> on the other hand, have resulted in an enormous spread in these parameters. As suggested by Griffin *et al.*<sup>18</sup> and by Cowern<sup>19</sup> the discrepancies in the values for  $D_I$  could be explained on the basis of trap-limited interstitial diffusion; however, no consensus has been reached until now about the nature of these intrinsic traps in silicon.

A more pressing uncertainty in modeling TED is the number of interstitials arising from the implant which contribute to the enhanced diffusion. It was proposed<sup>10</sup> that the implanted atom causes a net imbalance in the ion-generated population of interstitials and vacancies.<sup>7</sup> Upon annealing, interstitials and vacancies quickly recombine to restore the damaged lattice, leaving one atom per implanted ion which cannot be annealed out immediately. The supersaturation of interstitials during TED is thought to arise from this one excess interstitial per ion, rather than from the entire ion-generated distribution of interstitials; this has become known as the “+1” model. Although this simple model provides an estimate for the level of interstitials injected during TED, it has never been verified experimentally. Furthermore, it is not fully clear whether the excess interstitials emerge instantaneously from the initial distribution, or whether their rate of injection is limited by interstitial clustering.<sup>9</sup> Finally, modeling the evolution of interstitial damage requires detailed knowledge of the rate at which interstitials recombine, either at the surface or in the bulk, a process which is still poorly understood.

Another ambiguous feature of TED is the fact that the peak portion of implanted B profiles remains static and inactivated upon annealing when an apparent critical dopant concentration is exceeded,<sup>10,11</sup> as also demonstrated in Fig. 1. It was proposed<sup>10</sup> that this effect arises from the large supersaturation of B atoms in interstitial positions leading to an effective lowering of the equilibrium solubility limit of B in Si. Alternatively, the anomalous B diffusion was ascribed to the trapping of B at extended defects,<sup>9</sup> or was explained in terms of an enhanced coupling between B and neutral interstitials.<sup>20</sup> The latter model was based on the observation that the kink in the dopant profiles after TED appears to be correlated with the intrinsic carrier concentration. In a recent article on process simulations,<sup>21</sup> the rather unphysical assumption was made that the incomplete B activation results from the formation of immobile, isolated B interstitials through a kick-out reaction with Si interstitials. Each of the above explanations allows for a sufficient number of free parameters to enable fitting of the diffused dopant profiles through process simulations, a situation which calls for decisive experiments.

In the past years, many of the detailed aspects of TED have been investigated by utilizing dopant marker layers in diffusion experiments.<sup>22–35</sup> These experiments were designed to detect the effect of interstitial injection from a localized source (e.g., implantation damage, oxidizing surface) on well-separated dopant profiles. In the experiments presented in this article, diffusion studies using dopant superlattice structures were linked to damage measurements using transmission electron microscopy (TEM).<sup>36</sup> This combination has yielded a wealth of information about the mechanisms of TED, and has significantly improved our insights into the source of interstitials during TED, the diffusion behavior of interstitials in Si, and the mechanism through which B is immobilized during TED.

Several methods have been published through which the interstitial-enhanced dopant diffusion can be suppressed. A significant reduction in TED can be achieved by amorphiz-

ing the *c*-Si substrate prior to dopant implantation and annealing,<sup>37,38</sup> however, it has proven to be difficult to control the defect band located at the original amorphous Si (*a*-Si)/*c*-Si interface, which can result in increased junction leakage. Furthermore, additional interstitials will be emitted from the defect band during further thermal processing thus causing TED to persist. It has also been demonstrated that the TED of near-surface B implants can be greatly reduced by superimposing a high-energy (MeV) Si implant before annealing.<sup>39</sup> Although this reduction was originally ascribed to the trapping of interstitials at the stable dislocation damage formed by the deepest implant,<sup>39</sup> it is more likely caused by the excess vacancies in the near-surface region generated by the high-energy implant.<sup>40</sup> Again, implementation of this recipe for suppressing TED might be precluded by the detrimental effects of the buried damage layers. Recently, it has been reported that C coimplantation can be used to reduce TED of B.<sup>41,42</sup> This reduction has been attributed<sup>43–45</sup> to the fact that the implanted C provides a sink for excess interstitials during annealing. The efficacy of C coimplantation in suppressing TED is limited by the fact that the C needs to get its own interstitial damage in addition to the interstitials from the dopant implant.<sup>44</sup> It could therefore be more efficient to incorporate substitutional C in *c*-Si before implanting the dopant species, which is an additional subject of research in this article.

This article is organized as follows. Section II describes the experimental details of the present work. The complementary TEM and diffusion experiments are presented in Secs. III and IV, respectively. Section V elaborates on an interstitial-driven clustering mechanism of B. It is demonstrated in Sec. VI that incorporating substitutional C in *c*-Si is successful in suppressing TED. Furthermore, Sec. VI discusses in detail how the presence of C in Si is thought to affect the diffusion of interstitials in marker layer experiments and metal diffusion studies. In Sec. VII a Monte Carlo diffusion code is presented which was developed to enrich our understanding of the detailed defect-dopant interactions during annealing. Finally, to illustrate the improvements that have been made, Sec. VII shows how the present results have been implemented into a process simulator.

## II. EXPERIMENT

### A. Sample preparation

The present experiments were designed to investigate how implantation damage in silicon evolves during annealing, and how it affects the diffusion of dopant atoms. The structure and evolution of implantation damage was identified by means of cross-sectional and plan-view TEM. Dopant diffusion was measured with high sensitivity by using special marker layer structures grown by low-temperature molecular-beam epitaxy (MBE).<sup>46</sup> These structures consisted of 600-nm-thick films of Si grown on Si (100) substrates (FZ, P-doped to 1000  $\Omega$  cm), containing 10-nm-wide spikes of substitutional B. The dopant spikes were separated by  $\sim 100$  nm, with each spike containing  $1.5 \times 10^{12}$  or  $1.5 \times 10^{13}$  B/cm<sup>2</sup>.

Additional diffusion measurements were performed for B marker layers implanted into FZ Si wafers (*p*-type doping, 100  $\Omega$  cm, 100 orientation) using a tandem accelerator. The detailed preparation scheme has been given in Ref. 47. In brief, FZ wafers were amorphized at liquid-nitrogen temperature by implanting 0.5, 1, and 2 MeV Si at a dose of  $5 \times 10^{15}$ /cm<sup>2</sup> each. The amorphized layers were subsequently implanted with  $2.3 \times 10^{14}$ /cm<sup>2</sup>, 60 keV B and  $4 \times 10^{14}$ /cm<sup>2</sup>, 400 keV B. The implanted samples were annealed after implantation leading to regrowth of the amorphized layer through solid-phase epitaxy (SPE) and full activation of the implanted B, as ascertained from spreading resistance profiling (SRP).<sup>47</sup>

Damage and diffusion experiments were also carried out on FZ and MBE samples which were intentionally doped with relatively high levels of C or B. Samples with increased C contents were prepared using two methods. First, the amount of C incorporated in MBE-grown superlattices was enhanced by introducing acetylene gas in the MBE chamber through a leak valve. As measured by secondary-ion-mass spectroscopy (SIMS) at a sputtering rate of 12  $\text{\AA}$ /s using a 3 keV Cs<sup>+</sup> beam, the background C level increases from  $10^{18}$ /cm<sup>3</sup> for the standard growth conditions to  $2 \times 10^{19}$ /cm<sup>3</sup> for growth under an acetylene pressure of  $10^{-7}$  Torr. The C incorporation at the B doping spikes is increased by a factor of 3 due to growth interrupts. TEM analysis shows no carbon precipitation upon annealing the C-rich silicon layers at 1000  $^{\circ}$ C for 1 h, indicating that the incorporated C remains substitutional up to high temperatures.

In a second scheme for achieving C doping, MBE-grown superlattices and FZ Si(100) wafers were amorphized to a depth of 2  $\mu$ m at  $\sim 77$  K using 0.5, 1, and 2 MeV Si implants to a total fluence of  $1.5 \times 10^{16}$ /cm<sup>2</sup>. Some samples were implanted with C at multiple energies ranging from 10 to 400 keV with doses chosen to approximate a uniform C doping level to a depth of  $\sim 1$   $\mu$ m. Other samples were implanted at a single energy so as to obtain a buried peak of high C content. After the C implants samples were annealed in vacuum at 500  $^{\circ}$ C for 1 h, 600  $^{\circ}$ C for 2 h, and 790 or 900  $^{\circ}$ C for 15 min to regrow the *a*-Si layer by SPE and dissolve the implanted C in the *c*-Si lattice. It should be noted that C is known to regrow onto substitutional sites during SPE of *a*-Si for C levels as high as  $\sim 1$  at. %.<sup>48</sup>

Heavily boron-doped silicon substrates were prepared by the following procedure. Six FZ (100) silicon wafers (B doped, 1  $\Omega$  cm) were first oxidized in dry O<sub>2</sub> at 1000  $^{\circ}$ C to form a 20-nm-thick screen oxide. Boron was then introduced into five of these wafers by ion implantation of <sup>10</sup>B<sup>+</sup> at 120 keV to various doses, followed by annealing at 1050  $^{\circ}$ C for 2 h. This anneal accomplished two objectives: It removed all of the observable implantation damage caused by the B implant, and it diffused the implanted B profile uniformly over a considerable depth. The implantation and annealing conditions had been chosen with the help of the process simulator PROPHE<sup>49</sup> to produce B profiles that were uniform (within 10%) over a distance of at least 300 nm from the surface. The implanted <sup>10</sup>B doses were  $6 \times 10^{13}$ /cm<sup>2</sup>, and 2, 3, 4, and  $6 \times 10^{14}$ /cm<sup>2</sup>, producing boron concentrations [B] of 1, 3, 5,  $7 \times 10^{18}$ , and  $1 \times 10^{19}$ /cm<sup>3</sup>, respectively, in the uniform sur-

face region after the diffusion anneal. Spreading resistance measurements were used to verify the quoted B concentrations and depth distributions. The sixth oxidized wafer received no  $^{10}\text{B}$  implant and was used as a reference.

## B. Implants, annealing, and diffusion

Low-energy implants ( $<70$  keV) were performed by extracting negatively charged ions from a sputter source biased at the desired voltage, without net acceleration inside the tandem accelerator. The standard procedure to introduce near-surface implantation damage in silicon samples consisted of room-temperature implants of 40 keV  $\text{Si}^-$  at dose rates of  $(1.3 \pm 0.6) \times 10^{12}$  ions/cm $^2$ /s to total doses ranging from  $5 \times 10^{12}$  to  $5 \times 10^{14}$  ions/cm $^2$ . A typical B doping implant was done at room temperature using a 60 keV  $\text{B}_2$  beam at a dose of  $7.5 \times 10^{13}$ /cm $^2$ , which corresponds to implanting 30 keV B to a dose of  $1.5 \times 10^{14}$ /cm $^2$ .

After implantation, samples were chemically cleaned by successive rinsing with trichloroethylene, acetone, and methanol, followed by a standard RCA cleaning step. Prior to being annealed, samples received a 20 s dip in a 1:20 diluted solution of HF. Most anneals were carried out in a conventional tube furnace with a base vacuum pressure well below  $10^{-7}$  mbar. Samples were carried by a support wafer in a quartz boat and annealed in vacuum or under forming gas (85%  $\text{N}_2$ , 15%  $\text{H}_2$ , flow rate 1.5  $\ell$ /min). Varying between these two annealing ambients was found not to affect the present nonequilibrium damage and diffusion experiments to a measurable extent, provided that the furnace settings were changed to compensate for temperature shifts.<sup>50</sup> Other gas flow conditions have occasionally been used and are specified in this article where necessary.

The furnace temperature settings were carefully calibrated in separate runs using a thermocouple mounted at the exact location of the samples. Temperature differences between annealing in vacuum and under gas flow were measured to be as high as, for instance,  $\sim 40$   $^\circ\text{C}$  for a furnace setting temperature of 700  $^\circ\text{C}$ . The temperatures quoted in the remainder of this article are the calibrated values of the actual sample temperature during annealing, which are believed to be accurate to within 10  $^\circ\text{C}$ . Some samples were subjected to a rapid thermal annealing (RTA) step under forming gas flow. In that case, the temperature was calibrated to within 25  $^\circ\text{C}$  by measuring the rates of SPE regrowth of ion-beam-amorphized layers on Si(100) substrates.<sup>51</sup>

In order to study interstitial-enhanced diffusion, ion-damaged B superlattices were annealed under various thermal conditions. Boron depth profiles before and after diffusion were obtained by SIMS at a sputtering rate of 4  $\text{\AA}$ /s using 2 keV  $\text{O}_2^+$ . The time-averaged intrinsic B diffusivity  $\langle D_{\text{B}}^{\text{int}} \rangle$  was derived from each diffused doping spike using the optimization procedure described elsewhere.<sup>28,52</sup> The B spike confined to ion-damaged regions has been excluded in the diffusion analysis, as it is unclear *a priori* to what extent the diffusion of this spike is perturbed by the implantation damage.



FIG. 2. Cross-section high-resolution electron micrograph showing  $\{311\}$  habit plane, and typical image contrast of  $\{311\}$  defects.

## III. INTERSTITIAL INJECTION

### A. Results

This section presents TEM studies of the annealing behavior of ion-implanted FZ samples. Identical implantation and annealing conditions were used to study interstitial-enhanced diffusion in B marker layer structures (Sec. IV), which will enable a direct link between implantation damage and TED.

Figure 2 shows a cross-section electron micrograph of a FZ sample that was implanted with 40 keV Si,  $5 \times 10^{13}$ /cm $^2$  and annealed at 815  $^\circ\text{C}$  for 15 s using RTA. The high-resolution image of Fig. 2 clearly demonstrates the presence of a defect with a  $\{311\}$  habit plane. A series of cross-section images demonstrates that these defects are confined to the top 0.1  $\mu\text{m}$  surface region of the sample. Plan-view analysis shows a high concentration of elongated defects along (110) directions, see Fig. 3, and this appearance is consistent with the notorious “rodlike” or “ $\{311\}$  defects.”<sup>53</sup> These defects consist of an agglomeration of excess Si self-interstitials and are known to form in response to the nonequilibrium injection of interstitials resulting from oxidation,<sup>54</sup> electron bombardment,<sup>55</sup> or ion implantation.<sup>54,56</sup> Although  $\{311\}$  have recently been presented as a band of interstitials on a compact disk,<sup>56,57</sup> it is generally recognized that  $\{311\}$  interstitial clusters have an anisotropic, elongated shape. For a detailed discussion on the structural properties of  $\{311\}$  defects, the reader is referred to a recent review article by Takeda and co-workers.<sup>53</sup>

Cross-section and plan-view microscopy were combined to follow the evolution of  $\{311\}$  defects during annealing. As is clear from Fig. 3, the areal density of  $\{311\}$  defects drops by several orders of magnitude upon increasing the annealing time at 815  $^\circ\text{C}$  from 5 to 30 s. Simultaneously, the average length of the defects increases from roughly 5 to 20 nm. No defects were detectable for annealing times in excess of 5 min, suggesting complete damage dissolution. The quantitative measurements of defect density and average defect size, as summarized in Fig. 4, were used to calculate the number of interstitials contained in  $\{311\}$  defects.<sup>58</sup> Figure 5 shows

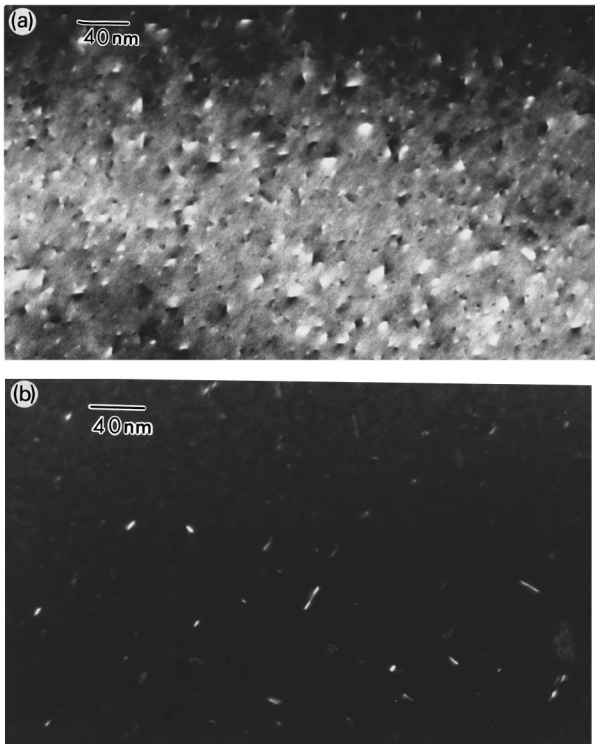


FIG. 3. Plan-view  $\langle 220 \rangle$  dark-field images of FZ silicon implanted with  $5 \times 10^{13}/\text{cm}^2$ , 40 keV Si after rapid thermal annealing at 815 °C for (a) 5 s, (b) 30 s.

that the areal interstitial density falls off exponentially with characteristic decay times ranging from  $\sim 40$  s at 815 °C to  $\sim 4$  h at 670 °C. It should be noted that the width of  $\{311\}$  defects could not be accurately measured for very short annealing times, while the statistics for the defect density are rather poor in the final stage of the  $\{311\}$  decay. These uncertainties could imply that the decay curves are not purely exponential as in Fig. 5, but are likely to be more convex instead. The decay rates derived from the exponential fits in Fig. 5 are reproduced in the Arrhenius graph of Fig. 6, showing an activation energy of  $3.8 \pm 0.2$  eV for the dissolution of  $\{311\}$  defects.

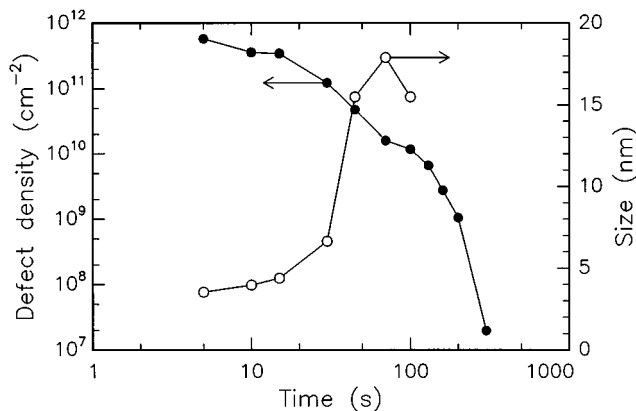


FIG. 4. Development of the density and the average length of  $\{311\}$  defects during annealing at 815 °C.

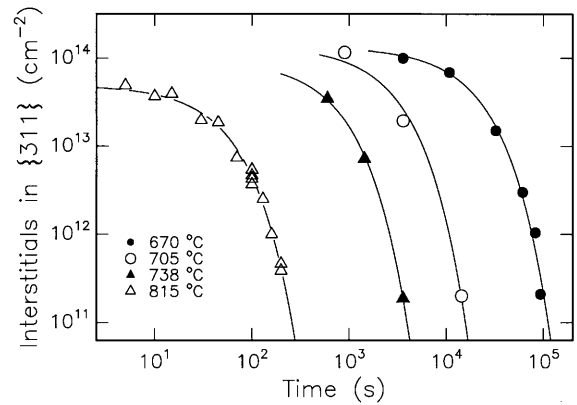


FIG. 5. Transmission electron microscopy measurements of the total interstitial areal density in  $\{311\}$  defects as a function of annealing time. Data are shown for float-zone Si samples which were implanted with  $5 \times 10^{13}/\text{cm}^2$ , 40 keV Si and annealed in forming gas at various temperatures.

It is noteworthy that the interstitial density in  $\{311\}$  defects in the initial annealing stages (Fig. 6) is similar to the implanted Si dose of  $5 \times 10^{13}/\text{cm}^2$ . Apparently, about one excess interstitial is formed for each implanted ion during annealing, in accordance with the +1 model. This observation is reconfirmed by measurements of the interstitial density as a function of ion dose in Fig. 7, which demonstrate a +1.4 dependence. It should be noted that no  $\{311\}$  defects were observed for implantation doses below  $\sim 5 \times 10^{12}/\text{cm}^2$ .

Figure 8 shows TEM measurements of the number of interstitials contained in  $\{311\}$  defects for samples which were doped with a high B background (see Sec. II for details). In similar experiments, FZ substrates were controllably doped with a uniform C level by ion-beam amorphization of the substrates followed by a series of C implants and epitaxial regrowth (Sec. II), and the results are shown in Fig. 9. Both types of samples were implanted with 60 keV Si,  $1 \times 10^{14}/\text{cm}^2$ , and annealed at 740 °C for 15 min. It is clear that the interstitial density in  $\{311\}$  defects decreases strongly with increasing B or C content. It thus appears that substitu-

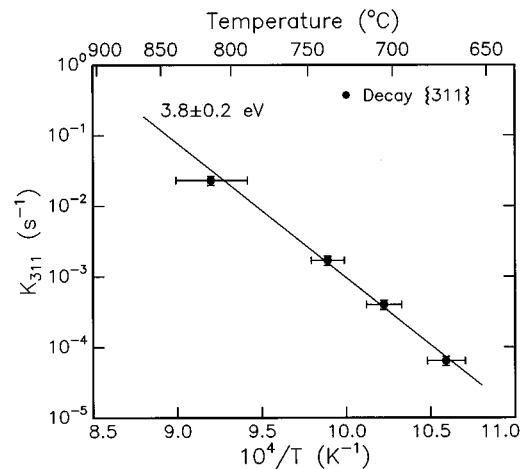


FIG. 6. Arrhenius graph of the time constant for  $\{311\}$  decay derived from the annealing curves in Fig. 5.

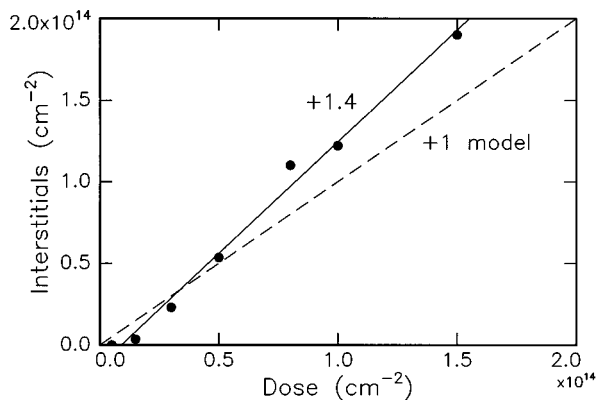


FIG. 7. Dose dependence of the number of interstitials in {311} defects during the early stages of annealing for 60 keV Si implants into float-zone silicon.

tional B and C reduce the formation of {311} defects; the implications of this observation are discussed extensively in Secs. V and VI of this article.

For implantation doses exceeding  $\sim 1 \times 10^{14}/\text{cm}^2$ , the damage annealing behavior in FZ samples becomes more complex in that dislocation loops are observed in addition to {311} defects.<sup>59,60</sup> The defects observed<sup>59</sup> upon annealing a  $1.5 \times 10^{14}/\text{cm}^2$ , 145 keV Si implant at 900 °C for 15 min are predominantly  $\frac{1}{3}[111]$  Frank loops frequently arranged in linear chains, suggesting that the loops may form from the 1- $\mu\text{m}$ -long rodlike defects seen at lower doses and shorter anneals.

## B. Discussion

In the dose range from  $5 \times 10^{12}$  to  $\sim 1 \times 10^{14}/\text{cm}^2$ , {311} defects are the only defect structures visible at the peak of the implant damage during annealing. The observation that the defect density drops while the average defect size increases (Fig. 4) is indicative of Ostwald ripening. This shows

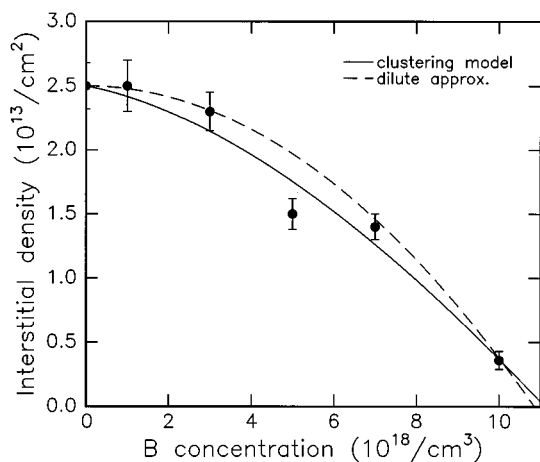


FIG. 8. Areal density of interstitials in {311} defects observed after annealing a  $1 \times 10^{14}/\text{cm}^2$ , 60 keV Si implant at 740 °C for 15 min, as a function of the B background doping level. The solid and dashed lines are fits to the data assuming interstitial trapping through B clustering.

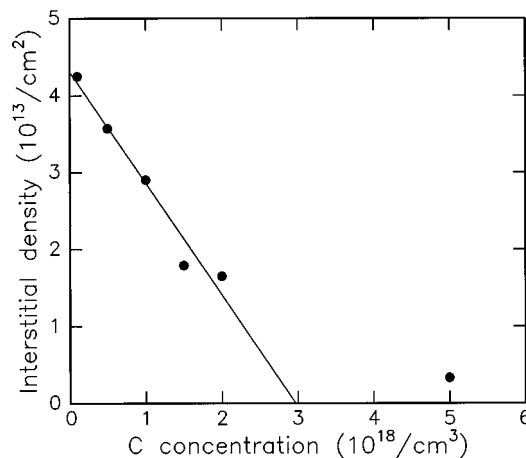


FIG. 9. Density of interstitials in {311} defects observed after annealing a  $1 \times 10^{14}/\text{cm}^2$ , 60 keV Si implant at 740 °C for 15 min, as a function of the C background doping level.

that interstitials are emitted from and recaptured by {311} defects, favoring the growth of larger (i.e., more stable) defects at the expense of smaller ones. However, as interstitials are lost from the damage region through diffusion to the surface or into the bulk of the material, the interstitial content held by {311} defects gradually decreases with time.

The presence of {311} defects implies that the interstitial concentration in the interior of the implanted sample is maintained above equilibrium. Hence, the interstitials which are gradually lost from the {311} defect distribution will give rise to enhanced dopant diffusion when they are captured by a dopant atom. Therefore, the evaporation of {311} defects will determine the time scale and the instantaneous strength with which TED takes place. It is shown in the following section that the time scales for enhanced B diffusion in marker layer experiments are indeed consistent with the {311} decay rates in Fig. 5. The presently derived activation energy for interstitial injection of  $3.8 \pm 0.2$  eV is in perfect agreement with the value of 3.7 eV, which was estimated from a collection of measurements of the time needed to saturate the enhanced diffusion of implanted B.<sup>11</sup>

Figures 6 and 7 show that the interstitial content of {311} defects is in remarkable agreement with the +1 model. Earlier experiments on the formation and growth of dislocation loops in ion-implanted Si have also indicated that the interstitial densities emerging during annealing are close to +1 approximation.<sup>61,62</sup> Monte Carlo simulations have been used to investigate how this simple rule of thumb can be reconciled with the complex interactions between interstitials and vacancies that govern the generation and annealing of ion damage.<sup>63</sup> Parts of these simulations are presented in Sec. VII A.

Figure 10 gives a tentative summary in the form of a “phase diagram” for {311} behavior, based on the observations for Si implants into FZ silicon in the energy range from 20 to  $\sim 150$  keV. For doses below the amorphization threshold, the defect processes are only weakly dependent on the initial damage level, so that the diagram can be mapped in terms of implantation dose versus annealing “strength.” At

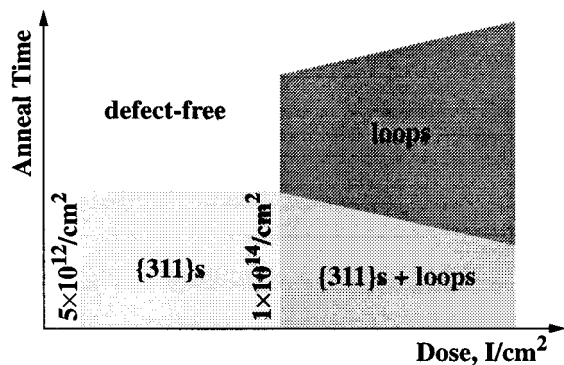


FIG. 10. Schematic diagram of the annealing behavior of {311} defects in relation to the implanted ion dose and the thermal annealing "budget."

implantation doses below  $5 \times 10^{12}/\text{cm}^2$ , no {311} defects are observed. This could indicate that the interstitial clusters formed from the implantation damage are too small to be detected by TEM. Alternatively, this threshold dose could reflect a nucleation barrier for the formation and growth of {311} defects. For doses in between  $5 \times 10^{12}/\text{cm}^2$  and  $1 \times 10^{14}/\text{cm}^2$ , {311} defects are the only visible defects and they evaporate for a sufficiently high thermal budget (i.e., annealing time and temperature). The evaporation rate at a given temperature is dependent on implantation dose and energy.<sup>60,64</sup> Above a threshold dose of  $\sim 10^{14}/\text{cm}^2$ , {311} defects undergo unfauling, leading to both Frank loops and perfect dislocations. Since these dislocations are more stable than {311} defects, significantly stronger annealing steps are needed to fully dissolve the dislocation damage. Further studies are necessary to identify how the time scales and strength of interstitial injection are affected by the transformation of {311} defects into dislocation loops.

#### IV. INTERSTITIAL DIFFUSION

##### A. Results

The injection of interstitials from {311} defects was detected by probing the broadening of B marker layers during annealing. It was verified that the annealing behavior of {311} defects in MBE material is quantitatively similar to the studies on FZ material presented in Sec. III, at least for the implant conditions presently used ( $5 \times 10^{13}/\text{cm}^2$ , 40 keV Si).

Figure 11 shows the as-deposited and diffused B doping profiles in MBE-grown superlattice structures. After implantation and annealing, each of the doping spikes has broadened well beyond the initial width of  $\sim 100$  Å as a result of the injection of interstitials. The broadening exceeds thermal diffusion for all markers and is most pronounced near the ion-implanted region. This behavior clearly demonstrates the diffusion mechanism underlying TED: Excess interstitials injected from the ion damage cause enhanced diffusion of the substitutional B markers. It is obvious that portions of the three doping markers closest to the surface remained immobile during annealing. The Gaussian fits in Fig. 11(b) show this particular shape can be reproduced by assuming that the markers consist of a mobile and an immobile component. This diffusion behavior very much reproduces the key fea-

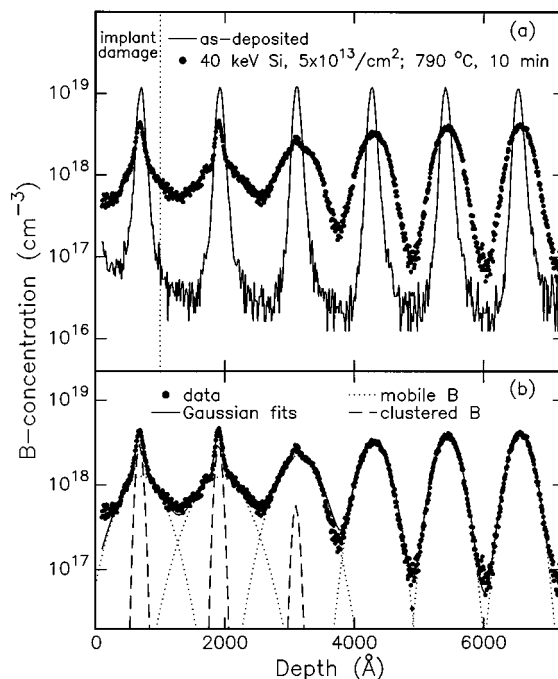


FIG. 11. (a) SIMS measurements of the B doping profile for an as-deposited superlattice and for a superlattice implanted with  $5 \times 10^{13}/\text{cm}^2$ , 40 keV Si and annealed in vacuum at 790 °C for 10 min. (b) Deconvolution of the doping markers into Gaussian diffusion profiles. Portions of the three near-surface markers are assumed to be immobile. The dashed line in (a) indicates the region in which stable {311} clusters are formed during annealing.

tures of TED as shown in Fig. 1. In Sec. V it is demonstrated that the static B peaks result from clustering of B driven by the interstitials.

Figure 12(a) shows the time-averaged intrinsic B-diffusivity  $\langle D_B^{\text{int}} \rangle$  as a function of depth derived from the diffusion profiles in Fig. 11(a) together with data obtained for 790 °C, 30 min annealing. The enhanced B diffusivity (i.e., the ratio of  $\langle D_B^{\text{int}} \rangle$  to the equilibrium diffusivity  $D_B^*$ ) is proportional to the amount by which the time-averaged local concentration of self-interstitials  $\langle [I] \rangle$  exceeds the equilibrium level  $[I^*]$ , as indicated on the right-hand-side axis of Fig. 12. The average interstitial concentration near the ion-implanted region drops from about  $200 \times [I^*]$  to about  $60 \times [I^*]$  upon increasing the annealing time from 10 to 30 min, indicating that the injection of interstitials has diminished after  $\sim 10$  min. The time-averaged interstitial diffusion profiles in Fig. 12(a) were modeled by calculating the time-average of a Gaussian peak broadening with a fixed effective interstitial diffusivity. Reasonable agreement was obtained by assuming  $\sim 1.3 \times 10^{-12} \text{ cm}^2/\text{s}$  for the diffusivity independent of annealing time.

The diffusion studies of Fig. 11 were repeated for B marker layers implanted in FZ Si wafers (see Sec. II and Ref. 47). Figure 13 shows SIMS profiles of the marker layer after preparation and after implantation with  $5 \times 10^{13}/\text{cm}^2$ , 40 keV Si followed by annealing at 790 °C for 10 min. The B peak near the damage region broadens considerably upon annealing, whereas the deepest peak remains unaffected. The broadening of the near-surface peak is remarkably asymmetric, which is presumably due to the fact that the clustering of

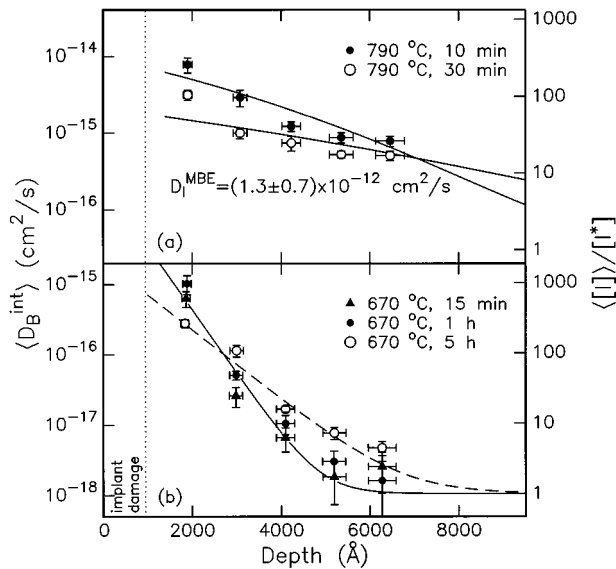


FIG. 12. Time-averaged intrinsic B diffusivity as a function of depth derived from the broadened portion of each doping marker after annealing at (a) 790 °C and (b) 670 °C for various times. The depth dependence of the diffusivity reflects the time-averaged interstitial diffusion profile (right-hand axis). Solid lines are (a) fits of the interstitial profile assuming an interstitial diffusivity of  $1.3 \times 10^{-12} \text{ cm}^2/\text{s}$  and (b) fits of exponential decays according to Eq. (3).

B suppresses diffusion near the damage source. By analyzing the broadening of the B peaks as a function of depth,<sup>47</sup> the interstitial diffusivity was estimated to be  $\leq 4 \times 10^{-12} \text{ cm}^2/\text{s}$ .

Figure 12(b) shows interstitial diffusion profiles obtained by measurements on MBE-grown superlattices at 670 °C. In contrast to the diffusion behavior at 790 °C, the interstitial supersaturation near the damage source and the decay length of the diffusion profiles remain unchanged during annealing for  $t \leq 1 \text{ h}$ . It thus appears that the interstitial diffusion profiles are initially stationary at 670 °C. Stationary profiles

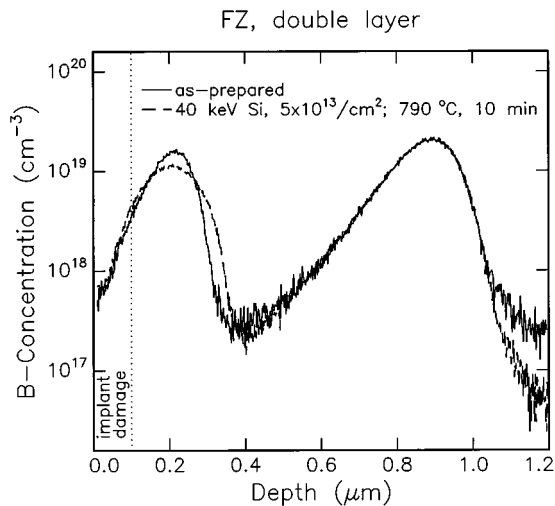


FIG. 13. SIMS measured B concentration profiles of FZ marker layers after preparation (Ref. 47) and after implantation with  $5 \times 10^{13}/\text{cm}^2$ , 40 keV Si followed by annealing in vacuum at 790 °C for 10 min.

with similar decay lengths were also observed for thermal annealing 550 °C up to  $\sim 150 \text{ h}$ .<sup>65</sup> The diffusion profile after annealing at 670 °C for 5 h deviates from this steady-state situation [see Fig. 12(b)], indicating that interstitials have diffused beyond the initial decay length.

## B. Discussion

The diffusion data in Figs. 11 and 12 indicate that the injection of interstitials lasts for  $\sim 10 \text{ min}$  at 790 °C and  $\sim 5 \text{ h}$  at 670 °C, and these time scales are consistent with the measured evaporation rate of {311} defects in Fig. 6. Therefore, it appears that the duration of interstitial injection is correlated with the evaporation of {311} defects, reconfirming the notion of Sec. III that {311} defects act as the source of interstitials during TED.

The profile of excess interstitials exhibits regular, diffusional broadening at 790 °C, and the diffusion constant  $D_I^{\text{eff}}$  was estimated to be  $\approx 1.3 \times 10^{-12} \text{ cm}^2/\text{s}$  for MBE material. Similar diffusion studies at 720 °C yield  $D_I^{\text{eff}} \approx 1.1 \times 10^{-13} \text{ cm}^2/\text{s}$ . The stationary interstitial profiles observed at 550 and 670 °C, on the other hand, indicate that the penetration depth of injected self-interstitials is limited by the capture at trapping centers in the material. Under these conditions, the time-averaged interstitial profile is given by the steady-state profile  $[I^{\text{ss}}(x)]$ ,<sup>19</sup>

$$[I^{\text{ss}}(x)] = [I^*] + ([I^0] - [I^*]) \exp(-x/L_I), \quad (3)$$

where  $[I^0]$  is the interstitial concentration at the source (assumed to be constant),  $x$  the distance from the source, and  $L_I$  a characteristic decay length related to the trap density  $[T]$  and the trapping radius  $a_T$  according to  $L_I = (4\pi a_T [T])^{-1/2}$ .

The solid line in Fig. 12(b) is a least-squares fit of Eq. (3) to the diffusion profiles for 15 min and 1 h, yielding  $L_I = 480 \pm 50 \text{ \AA}$  and  $[I^0]/[I^*] = (7.7 \pm 3.8) \times 10^3$ .<sup>66</sup> The density of traps in the MBE-grown superlattice can be estimated from the value for  $L_I$  by taking  $a_T$  equal to the interatomic distance ( $a_T = 2.35 \text{ \AA}$ ), yielding  $[T] = (1.5 \pm 0.2) \times 10^{17}/\text{cm}^3$ . The vacancy level in our MBE-grown samples is below the detection limit of positron annihilation spectroscopy ( $5 \times 10^{15}/\text{cm}^3$ ),<sup>67</sup> suggesting that the dominant traps are associated with impurities. Indeed, the background C level  $[C_{\text{MBE}}]$  in the MBE superlattices is  $\sim 10^{18}/\text{cm}^3$ , and it is shown below (Sec. VI) that substitutional C is a strong trap for self-interstitials. The fact that the above estimate for  $[T]$  is slightly lower than  $[C_{\text{MBE}}]$  could indicate that not all carbon is active as a trap, or that  $a_T$  is smaller than  $2.35 \text{ \AA}$  due to a small activation barrier to trapping ( $\sim 0.15 \text{ eV}$ ).

For diffusion times exceeding  $t_c = 1 \text{ h}$ , the interstitials migrate beyond the trapping length at 670 °C. This effect either arises from the saturation of centers available for interstitial trapping,<sup>19</sup> or from the reemission of interstitials initially bound to traps. The effective interstitial diffusivity  $D_I^{\text{eff}}$  in this regime can be estimated from the criterion that  $\sqrt{D_I^{\text{eff}} t_c} \geq L_I$ , yielding  $D_I^{\text{eff}} \approx 6.4 \times 10^{-15} \text{ cm}^2/\text{s}$ . The present values for  $D_I^{\text{eff}}$  are in good agreement with our previous studies on oxidation-enhanced diffusion in MBE-grown superlattices,<sup>28</sup> but are orders of magnitude lower than diffusivities derived from metal diffusion studies<sup>15,68</sup> and exhibit



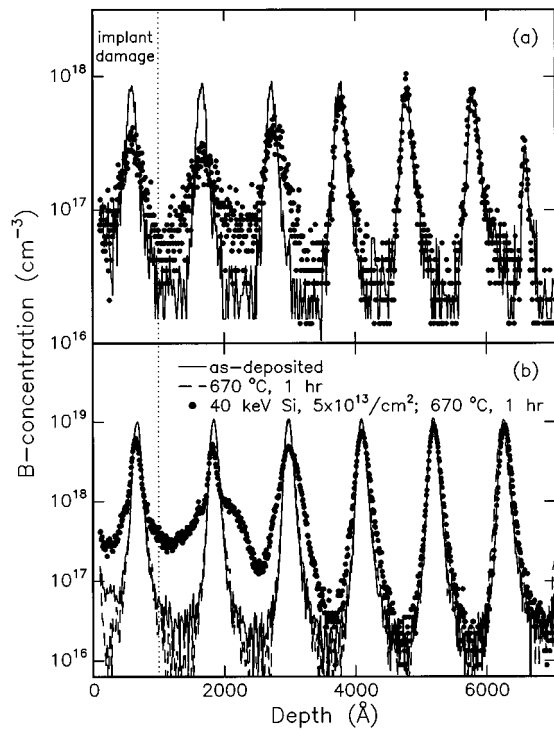


FIG. 14. Boron diffusion profiles after TED ( $5 \times 10^{13}/\text{cm}^2$ , 40 keV Si implant; 670 °C, 1 h anneal) for delta-doping superlattices with B peak concentrations of (a)  $10^{18}/\text{cm}^3$  and (b)  $10^{19}/\text{cm}^3$ .

a higher effective activation energy of  $3.8 \pm 0.5$  eV compared to 1.2–1.8 eV.<sup>15,68</sup> These discrepancies can be reconciled on the basis of trap-limited interstitial diffusion resulting from the high carbon concentration in the presently studied MBE material. It should be noted that this carbon level is not necessarily representative for the material quality obtained by MBE growth.<sup>19,27</sup> It is remarkable that the FZ marker layers (Fig. 13) give similar values for  $D_I^{\text{eff}}$ , whereas the C content of FZ silicon is expected to be well below  $10^{17}/\text{cm}^3$ . Presumably, additional impurities or vacancy-type defects were introduced during the amorphization and/or regrowth steps in preparing the FZ marker layers, thereby hampering interstitial diffusion. Section VI discusses in detail how C is thought to affect the diffusion of Si self-interstitials.

## V. BORON CLUSTERING

### A. Results

The marker layer experiments of Fig. 11 show that a considerable portion of the B spike located next to the damage region remains immobile during annealing, whereas the deeper B spikes exhibit regular broadening without a signature of immobile B. Figure 14 demonstrates how this effect changes upon reducing the maximum B level in the superlattice from  $10^{19}$  to  $10^{18}/\text{cm}^3$ . Transient diffusion was induced in both samples by annealing a 40 keV Si,  $5 \times 10^{13}/\text{cm}^2$  implant at 670 °C for 1 h. Analysis of the diffused spikes shows that the interstitial diffusion profiles in both samples are nearly identical. Yet, the diffused profile in the high concentration sample [Fig. 14(b)] shows a clear distinction between mobile and immobile B in the second dop-

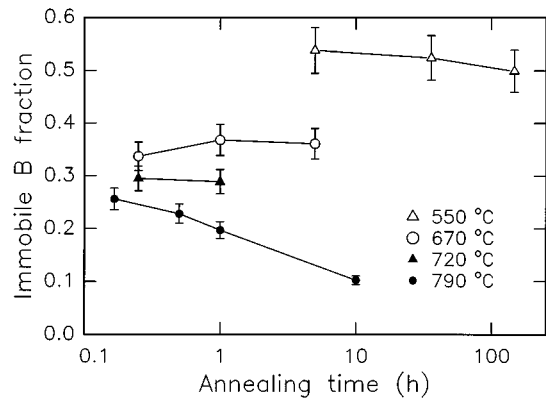
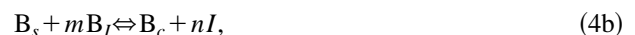


FIG. 15. Temporal evolution at 550, 670, 720, and 790 °C of the clustered B fraction in the second doping marker, derived from Gaussian fits to diffusion profiles as in Fig. 11(b).

ing spike, whereas this dual behavior is not observed in the low concentration sample. Figure 15 shows that the immobile fraction of the second B doping spike in high-concentration samples ( $10^{19}$  B/cm<sup>3</sup>) ranges from  $\sim 0.5$  at 550 °C to  $\sim 0.25$  at 790 °C. The immobile fraction remains at the initial level upon continued annealing in the temperature range from 550 to 720 °C, whereas it decays on a time scale of  $\sim 10$  h at 790 °C.

### B. Discussion

The observations made on the basis of Fig. 14 indicate that the formation of immobile B requires a relatively high concentration of both interstitials and substitutional B. Apparently, the clustering of multiple B atoms is facilitated when sufficient B atoms are driven out of solution by Si self-interstitials. Electrical measurements show that the immobile B peaks are electrically inactive, which is indeed consistent with B clustering. Presumably, the clustering process involves mobile B atoms  $B_I$  and a possible set of reactions which describes the generation and clustering of  $B_I$  is given by



where  $B_c$  refers to immobile clusters containing  $m+1$  B atoms, and  $n$  is the number of interstitials ejected upon clustering to allow for stress relief. While reaction (4a) sustains the interstitial-enhanced diffusion of  $B_s$ , reaction (4b) provides a channel through which  $B_s$  becomes immobile at concentrations below the solubility limit, as observed. Figure 15 demonstrates that the B clusters are metastable and dissolve upon continued annealing at sufficiently high temperatures.

In an attempt to further identify the clustering mechanism, the diffusion behavior of an ion-implanted B superlattice annealed at 670 °C for 1 h was numerically modeled (Fig. 16). The diffusivity  $D_{B_s}$  of unclustered, substitutional B is enhanced by the local interstitial concentration  $[I]$  according to

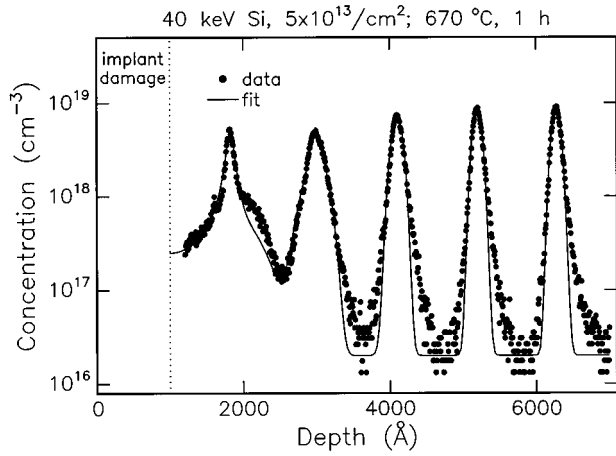


FIG. 16. SIMS measurements (solid circles) of an ion-damaged B marker superlattice annealed at 670 °C for 1 h and the corresponding best fit (solid line) obtained by modeling interstitial-enhanced clustering of B.

$$D_{B_s} = \left( 1 + \beta \frac{p}{n_i} \right) D_B^x \frac{[I]}{[I^*]}, \quad (5)$$

where  $D_B^x = D_B^*/(1 + \beta)$ ,  $p = n_i$  for  $[B_s] < n_i$ , and  $p = [B_s]$  for  $[B_s] > n_i$ ,<sup>28</sup> with  $n_i$  the intrinsic carrier concentration and  $\beta = 0.2$  at 670 °C. Assuming that the pairing reaction of  $B_I$  and  $B_s$  is diffusion-limited, the formation of  $B_c$  clusters is governed by the following rate equation:

$$\frac{d[B_c]}{dt} = 4\pi a_c D_{B_I} [B_I] [B_s], \quad (6a)$$

where  $D_{B_I}$  is the diffusivity of  $B_I$ ,  $a_c$  is the pairing radius, and  $[B_c]$  and  $[B_I]$  are the concentrations of  $B_c$  and  $B_I$ , respectively. It should be noted that Eq. (6a) ignores the dissolution of clusters for  $T = 670$  °C in agreement with Fig. 15. The product  $D_{B_I} [B_I]$  reflects the B diffusion capacity and is equal to  $D_{B_s} [B_s]$ . Therefore, Eq. (6a) can be rewritten as

$$\frac{d[B_c]}{dt} = 4\pi a_c D_{B_s} [B_s]^2. \quad (6b)$$

The concept of Eq. (6b) can be readily extended to include higher order clustering reactions (e.g., pairing of  $B_I$  and  $B_c$ ).

The above approach was used to calculate the evolution of the as-deposited B superlattice profile in response to diffusion and clustering of B under the wind of interstitials. The interstitial concentration  $[I(x)]$  was fixed at the steady-state profile of Eq. (3) using the fitted values for  $[I^0]$  and  $L_I$  [Fig. 12(b)]. Satisfactory agreement was obtained by taking two clustering reactions into account (i.e.,  $B_I$ - $B_s$  and  $B_I$ - $B_c$  pairing), both with the same pairing radius  $a_c$ . The solid line in Fig. 16 represents the best fit to the diffusion data using  $a_c = 0.5$  Å, a value which seems reasonable in comparison to the interatomic distance in Si. Similar values were derived from analyzing data for diffusion at 670 °C, 15 min. Modeling the data for 720 and 790 °C would require more elaborate calculations to account for the non-stationary interstitial profiles, which is beyond the scope of this simple analysis. Yet, the results in Fig. 16 suggest that the static peaks ob-

served in the marker experiments can indeed be attributed to the clustering of a few (two or three) B atoms induced by excess Si interstitials.

This notion is further corroborated by the result of Fig. 8, which illustrates that increasing the B background concentration leads to a reduction in the number of interstitials contained in  $\{311\}$  defects during annealing. Presumably, this interstitial loss arises from the trapping of interstitials during the B clustering process.<sup>69</sup> The data in Fig. 8 can be analyzed in detail by assuming that a fixed density of interstitials,  $[I_{311}]_0$ , is shared in quasiequilibrium between an unsaturable sink  $S$  (i.e.,  $\{311\}$  defects) and a population of small B clusters (assumed to be  $B_I$ - $B_s$  pairs). This assumption implies that

$$[B_I] = k_1 [B_s], \quad (7a)$$

$$[B_I B_s] = k_1 k_2 [B_s]^2, \quad (7b)$$

with  $k_1 = \exp(-\Delta E/kT)$  and  $k_2 = [N_s]^{-1} \exp(E_2/kT)$ . Here  $\Delta E$  denotes the energy difference between an interstitial trapped at a sink and an interstitial paired with a B atom,  $k$  is Boltzmann's constant,  $N_s$  is the Si atom density ( $5 \times 10^{22}/\text{cm}^3$ ), and  $E_2$  is the effective binding energy between two B atoms in a  $B_I$ - $B_s$  pair. The areal density of interstitials trapped by one or more B atoms is given by

$$[I_{\text{trap}}] = \Delta X ([B_I] + [B_I B_s]), \quad (8)$$

where  $\Delta X$  is the width of the region in which interstitials and B atoms interact, which should be roughly equal to the width of the as-implanted damage peak. Equations (7) and (8) yield the following expression which describes the  $\{311\}$  interstitial density  $[I_{311}]$  as a function of the total B concentration  $[B_{\text{tot}}]$ :

$$\frac{[I_{311}]_0 - [I_{311}]}{\Delta X} = \frac{[B_{\text{tot}}]}{2} \frac{k_1^2 - 1}{8k_1 k_2} \left[ 1 - \left( 1 + \frac{8k_1 k_2}{(k_2 + 1)^2} [B_{\text{tot}}] \right)^{1/2} \right]. \quad (9)$$

Equation (9) was fitted to the data in Fig. 8 yielding  $\Delta X = 500$  Å,  $\Delta E = 0.3$  eV, and  $E_2 = 0.9$  eV for the free parameters. Also shown is a quadratic model which is obtained from the above equations in the limit of dilute interstitial concentrations.<sup>69</sup> It is obvious that the above model for interstitial trapping during B clustering satisfactorily reproduces the measurements in Fig. 8.

The  $B_I$ - $B_s$  pair has been shown by deep-level transient spectroscopy (DLTS) to be stable up to temperatures of at least 400 °C.<sup>70</sup> Diffusion anomalies in earlier marker layer experiments<sup>71</sup> were also explained in terms of  $B_I$ - $B_s$  pair formation,<sup>72</sup> although the evidence was not as obvious as in the present experiments. The pairing reaction has been successfully applied in modeling TED for a small variety of implant and diffusion conditions.<sup>73</sup> Recent first-principles calculations<sup>74</sup> have been used to identify the atomic structure of the  $B_I$ - $B_s$  pair, and the activation barrier  $H_{\text{br}}$  to breaking this pair into two separate  $B_s$  atoms and one  $I$  was determined to be  $\sim 3$  eV. To first order, the average time  $\tau_{\text{br}}$  for dissolving a  $B_I$ - $B_s$  pair can be estimated on the basis of the

activation barrier by assuming  $\tau_{br}=10^{-13} \exp(H_{br}/kT)$  s. This yields  $\tau_{br}=16$  s at 790 °C, which is much shorter than the measured dissolution time of  $\sim 10$  h (see Fig. 15). This suggests that higher-order, more stable B–B agglomerates are involved in the clustering process.

The present observations support the earlier suggestion<sup>10</sup> that interstitial-driven B clustering might be responsible for the fact that the peak of implanted B profiles is static during TED and remains electrically inactive (see Fig. 1). The static B peak was observed<sup>10</sup> to dissolve on a time scale of  $>4$  h during post-TED annealing at 800 °C, which is indeed consistent with the data in Fig. 15. The present study also shows that the pinning of the B concentration during TED does not necessarily require the presence of extended defects such as rodlike defects or stacking faults, in contrast to what was proposed in the literature.<sup>9</sup> Furthermore, earlier studies<sup>20</sup> have pointed out that the demarcation level between mobile and immobile B appears to be correlated with the intrinsic carrier concentration  $n_i$ . This observation has occasionally been used as a reference point in process simulations to model the immobile B fraction during TED. However, the present study has shown that the demarcation levels may vary from spike to spike within one single sample (see, for instance, Fig. 11), which implies that the apparent correlation with  $n_i$  is fortuitous.

Finally, the present data indicate that Si self-interstitials become incorporated into the B clusters (i.e., when  $n < m$ ), leading to a local reduction in the interstitial concentration. This feature is further supported by *in situ* electron microscopy measurements.<sup>75</sup> It is noteworthy in this respect that the annealing of shallow B implants was found not to be accompanied by the formation of {311} defects, while TED remained.<sup>76</sup> In this case, the interstitial content is presumably reduced to below the threshold for {311} defect formation as a result of the consumption of interstitials by B clustering, combined with an increased interstitial loss due to the surface proximity.

In the present marker layer experiments, the flux of interstitials is not detectably perturbed by the clustering process. This is evident from, for instance, the fact that the interstitial diffusion profile at 670 °C is not significantly affected upon reducing the peak B concentration by one decade (Fig. 14). One explanation is that the level of trapped interstitials is too low to affect the interstitial population in the local vicinity of the B doping spike. Alternatively, recent superlattice studies seem to indicate that B clustering is initiated during the very early interstitial ‘burst’ of TED, before the {311}-controlled diffusion process is established.<sup>77</sup>

## VI. CARBON SUPPRESSING TRANSIENT ENHANCED DIFFUSION

### A. Results

On the basis of interstitial diffusion data it was speculated in Sec. IV B that C could act as a trap for Si self-interstitials. To investigate this notion in more detail, the effect of C doping on interstitial-enhanced B diffusion was studied by growing two different B superlattices by MBE (see Sec. II): one with a background C level of  $10^{18}/\text{cm}^3$

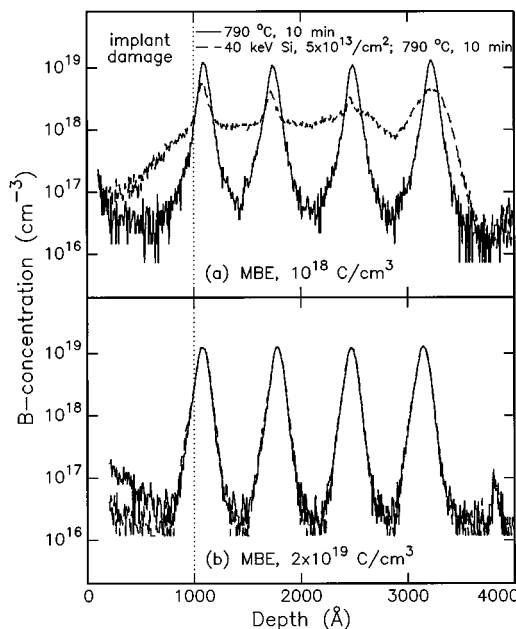


FIG. 17. Secondary-ion-mass spectrometry measurements of B diffusion profiles in MBE-grown superlattices containing substitutional C levels of (a)  $10^{18}/\text{cm}^3$  and (b)  $2 \times 10^{19} \text{ C}/\text{cm}^3$ . Profiles are shown for unimplanted and ion-damaged ( $5 \times 10^{13}/\text{cm}^2$ , 40 keV Si) superlattices after diffusion at 790 °C for 10 min.

grown under standard conditions, and one with an intentionally raised C level of  $2 \times 10^{19}/\text{cm}^3$  grown under a background acetylene pressure of  $10^{-7}$  Torr. Figure 17 shows SIMS measurements of the B profiles for unimplanted and implanted ( $5 \times 10^{13}/\text{cm}^2$ , 40 keV Si) superlattices after annealing. The B diffusion in the superlattice containing  $10^{18} \text{ C}/\text{cm}^3$  [Fig. 17(a)] is strongly enhanced with respect to thermal diffusion, and the behavior is similar to the previous superlattice measurements. The B diffusion in the ion-damaged superlattice with  $2 \times 10^{19} \text{ C}/\text{cm}^3$  [Fig. 17(b)], on the other hand, shows no significant enhancement relative to thermal diffusion. TEM micrographs demonstrate that the formation of {311} interstitial defects is fully suppressed in C-rich Si samples. This illustrates that the effect of C is to eliminate the source of TED, rather than to limit B diffusion by trapping the dopant atoms.

Figure 18 compares TED for a  $1.5 \times 10^{14}/\text{cm}^2$ , 30 keV B implant in C-lean FZ silicon (prepared by amorphization and SPE) and C-rich FZ silicon with a uniform level of  $4\text{--}6 \times 10^{18} \text{ C}/\text{cm}^3$  in the near-surface region (prepared by amorphization, C implantation, and SPE; see Sec. II). The diffused B profiles in the C-lean reference sample exhibit all the features characteristic to TED (see Fig. 1): Boron in the tail of the implanted profile has undergone enhanced diffusion over a distance of  $\sim 700$  Å upon annealing at 800 °C for 35 min, while the peak portion of the profile above  $10^{18}/\text{cm}^3$  has remained immobile due to the clustering of B driven by the excess interstitials. The diffusion behavior for the C-rich substrate is very different, as shown in Fig. 18(b). First, the diffusion length of B in the tail of the B profile stays well below  $\sim 700$  Å at both 800 and 950 °C. In addition, there is no pronounced signature of immobile B in the peak of the

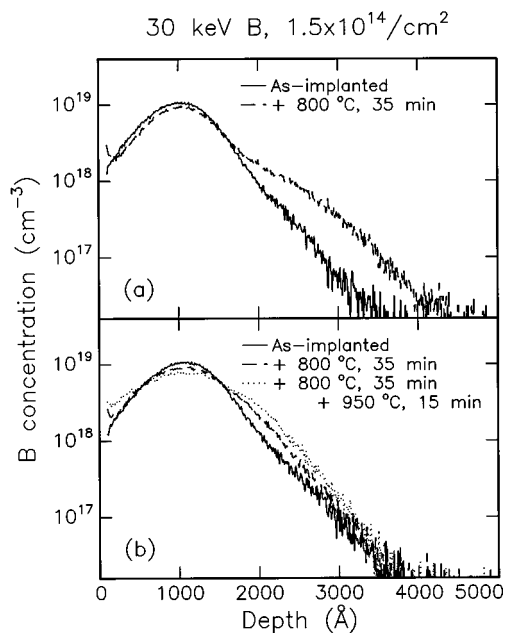


FIG. 18. SIMS measurements of B profiles after implantation ( $1.5 \times 10^{14}/\text{cm}^2$ , 30 keV B) and after subsequent annealing. Prior to B implantation, the float-zone Si sample in (b) was amorphized to a depth of  $2 \mu\text{m}$  by Si ion implantation, enriched with C by multiple implants to a level of  $4\text{--}6 \times 10^{18}/\text{cm}^3$  over  $1 \mu\text{m}$ , and regrown at  $500 \text{ }^\circ\text{C}$  for 1 h,  $600 \text{ }^\circ\text{C}$  for 2 h, and  $900 \text{ }^\circ\text{C}$  for 15 min. Sample (a) was prepared as sample (b), but without the C implants.

profile. Again, this demonstrates that C acts as traps for interstitials thereby suppressing both the enhanced B diffusion and the interstitial-driven clustering of B. In Fig. 19 the as-prepared and diffused C profiles are compared, which shows that a considerable portion of the C has diffused from the peak of the B implant to a depth of  $\sim 2000 \text{ \AA}$  after the high-temperature anneal. This indicates that C diffusion is enhanced by the injected interstitials, as is discussed in Sec. VI B.

The spreading resistance measurements of Fig. 20 show that the major part ( $\sim 80\%$ ) of the B profile is electrically active after the  $950 \text{ }^\circ\text{C}$  annealing step. In addition, Hall measurements on B profiles in *n*-type, C-rich substrates show that the electrically active fraction after diffusion at  $800 \text{ }^\circ\text{C}$  is

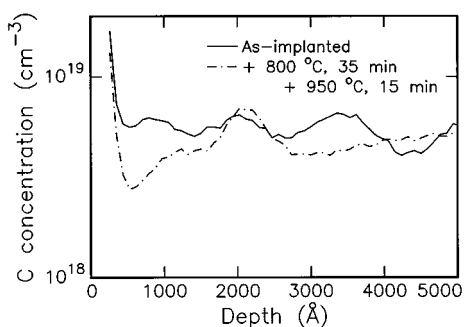


FIG. 19. Carbon depth profiles in C-rich FZ silicon [as Fig. 18(b)] after preparation of the sample, and after annealing an implant of  $1.5 \times 10^{14}/\text{cm}^2$ , 30 keV B at  $800 \text{ }^\circ\text{C}$  for 35 min and  $950 \text{ }^\circ\text{C}$  for 15 min.

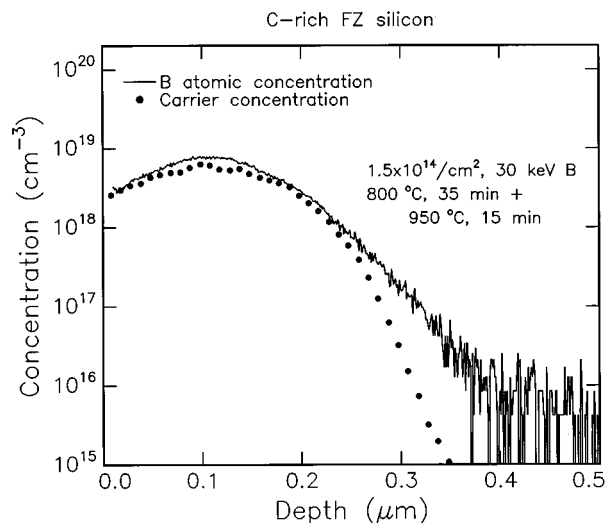


FIG. 20. Comparison of atomic and electrical B profiles in *p*-type, C-rich FZ silicon [as Fig. 18(b)] obtained after annealing an implant of  $1.5 \times 10^{14}/\text{cm}^2$ , 30 keV B at  $800 \text{ }^\circ\text{C}$  for 35 min and  $950 \text{ }^\circ\text{C}$  for 15 min.

approximately 60% and increases to  $\sim 85\%$  upon further annealing at  $950 \text{ }^\circ\text{C}$ , consistent with Fig. 20. The sheet resistance is 800 and  $620 \Omega/\square$  after annealing at 800 and  $950 \text{ }^\circ\text{C}$ , respectively. Comparable values were found for B profiles implanted into FZ substrates and annealed under the same conditions. These electrical measurements therefore show that the presence of C and/or C-interstitial agglomerates does not deteriorate the doping efficiency to unacceptable levels; however, preliminary ion-implanted diode structures prepared in wafers with relatively high C concentrations indicate enhanced junction leakage. This is in line with electrical measurements on C-implanted Si samples.<sup>78,79</sup> Further studies are required to investigate whether C incorporation in silicon precludes the formation of high-quality devices.

In order to assess the details of how C affects the flux of interstitials from a near-surface implant, superlattice structures were prepared which contain a nonuniform profile of substitutional C. To this end, MBE-grown B-doped *c*-Si superlattices were amorphized to a depth of  $2 \mu\text{m}$ , implanted with 115 keV C to a dose of  $9 \times 10^{13}/\text{cm}^2$ , and thermally regrown. Figure 21 shows the B and C profiles in C-rich superlattices (CSPE) and reference superlattices without C (SPE) after implantation and annealing. The injection of interstitials from the ion damage in sample SPE leads to diffusion and clustering of the B markers near the damage source. Figure 21(b) shows that the  $10^{18} \text{ C}/\text{cm}^3$  in sample SPE has redistributed under the injection of interstitials, analogous to the result of Fig. 19. The decoration of the B peaks with C could indicate that part of the mobile C is gettered at the B clusters. The substitutional C which was incorporated into superlattice CSPE consists of a peak of  $5 \times 10^{18}/\text{cm}^3$  at a depth of  $\sim 3000 \text{ \AA}$  [Fig. 21(b)]. Figure 21(a) shows that the injection of interstitials in sample CSPE also enhances B diffusion, but the broadening of the B peaks in the C-rich region is much less pronounced than in reference sample SPE.

Figure 22 summarizes the values for  $\langle D_B^{\text{int}} \rangle$  as a function

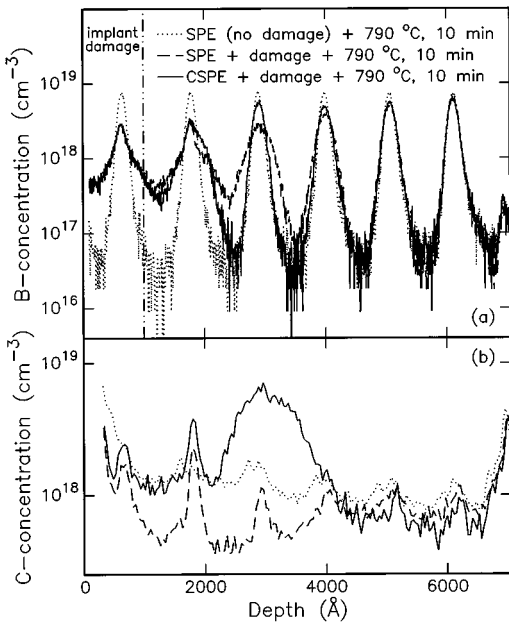


FIG. 21. SIMS measurements of (a) boron and (b) carbon depth profiles after diffusion at 790 °C for 10 min. CSPE refers to a MBE-grown B doping superlattice which was amorphized using Si implants, implanted with 115 keV C to a dose of  $9 \times 10^{13}/\text{cm}^2$ , and regrown at 500 °C for 1 h, 600 °C for 2 h, and 790 °C for 15 min. SPE was prepared as CSPE, but without the C implantation step. The damaging implant consisted of  $5 \times 10^{13}/\text{cm}^2$ , 40 keV Si.

of depth derived from the diffusion profiles in Figs. 11 and 21(a). The interstitial diffusion profile in sample SPE is significantly steeper than in the as-grown MBE sample, indicating a lower interstitial diffusivity. This suggests that the amorphization and/or SPE-regrowth steps have raised the level of interstitial traps in the superlattice. One possible mechanism could be the knock-on of carbon from deposited hydrocarbons on the sample surface during the relatively long ( $\sim 1$  h) amorphizing implant at liquid-nitrogen temperature. In addition, vacancy-type defects could have been introduced during SPE. The deviation between the diffusion

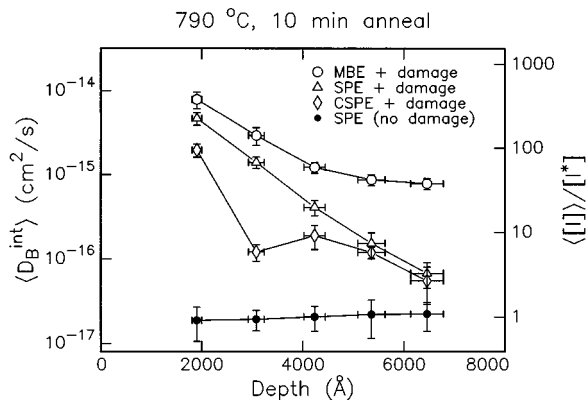


FIG. 22. Depth dependence of the intrinsic B diffusivity showing the effect of solid-phase epitaxy and C incorporation on the interstitial diffusion profile in MBE-grown superlattices. Data were obtained by analyzing the B diffusion profiles in Figs. 11(a) and 21.

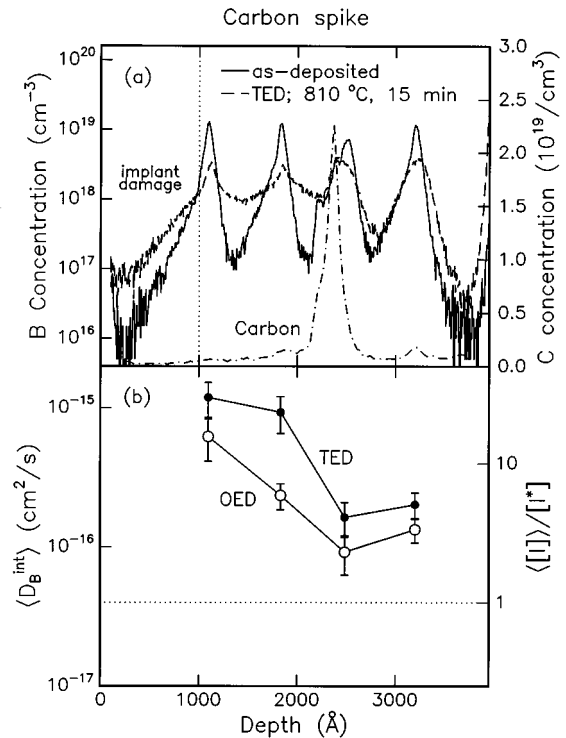


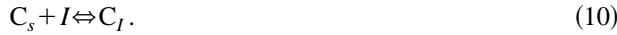
FIG. 23. (a) Boron diffusion profiles and (b) intrinsic B diffusivities for a MBE-grown superlattice containing a buried spike of substitutional C. Transient enhanced diffusion (TED) was induced by annealing a  $5 \times 10^{15}/\text{cm}^2$ , 40 keV Si implant at 810 °C for 15 min in vacuum. Oxidation enhanced diffusion (OED) was induced by repeating the same diffusion anneal for an unimplanted sample in a dry oxygen ambient.

profiles for samples SPE and CSPE demonstrates that the interstitial-enhanced diffusion of B is reduced by a factor of  $\sim 10$  at the peak of the C profile ( $\sim 3000$  Å deep). Beyond a depth of  $\sim 4500$  Å, however, the values for  $\langle D_B^{\text{int}} \rangle$  are nearly identical for both samples, indicating that the interstitial diffusion profile is only perturbed in the local vicinity of the incorporated C.

Figure 23 shows measurements of TED and oxidation-enhanced diffusion (OED) for a B-doped superlattice which contains a narrow C spike at a depth of  $\sim 2300$  Å. This structure was grown by briefly leaking  $\text{C}_2\text{H}_2$  into the MBE chamber in between the growth of the second and third B doping spike. As is obvious from the diffusion enhancements in Fig. 23(b), the implantation damage is a more efficient source for interstitials at 810 °C than the oxidizing surface. For both TED and OED, the third B spike shows significantly less broadening than the two spikes adjacent to the source of interstitials. In particular, the interstitial-enhanced diffusion is fully suppressed at the wing of the third doping spike that is contained within the buried C spike [see Fig. 23(a)]. On the other hand, the deepest marker layer exhibits at least as much broadening as the preceding spike, and the diffusion is a factor of 5 above  $D_B^*$ . Analogous to the results in Figs. 21 and 22, this indicates that the incorporation of C leads to a local reduction of the interstitial concentration without fully obstructing the flow of interstitials to the bulk of the material.

## B. Discussion

The results in the previous subsection have shown that raising the C concentration in Si from  $10^{18}$  to  $10^{19}/\text{cm}^3$  reduces the strength of interstitial-enhanced B diffusion. The straightforward explanation is that the interstitials driving TED are captured by substitutional C ( $C_s$ ) through the following well-known replacement reaction:<sup>80,81</sup>



The thus formed highly mobile  $C_I$  complex can pair with another substitutional C atom to yield a more stable complex ( $C_I C_s$ ),<sup>82,83</sup>



The ability of  $C_s$  to absorb interstitials is believed to play a crucial role in the coprecipitation of C and oxygen in Si at high temperatures,<sup>84</sup> although the detailed kinetics of this process are still under debate.<sup>85–87</sup> The formation of  $C_I$  pairs through the replacement reaction of Eq. (10) reduces the amount of interstitials available for pairing with substitutional B, thereby lowering the B diffusivity. The density of interstitials that is bound in  $\{311\}$  defects in the early annealing stages of TED was found to decrease linearly with increasing C level (Fig. 9), consistent with C–I pairing.

In the case of an initially uniform C distribution, the continuous exchange between C and I will impose a gradient in  $C_I$  which follows the diffusion profile of I. Since  $C_I$  is highly mobile,<sup>81,84</sup> this gradient will result in a net transport of C from the ion-implanted region to the adjacent region, as observed in Fig. 19. For comparison, it has been shown that the injection of interstitials during P in-diffusion yields a similar diffusion behavior in the near-surface region of C-rich Si samples.<sup>88</sup> In the case of a localized C peak (Figs. 21–23), the interstitials that are paired with C will be liberated when  $C_I$  diffuses out of the high-concentration region. This explains why the presence of C only causes a local reduction in the B diffusivity without fully suppressing the interstitial population at greater depths.

In addition to the effects of C–I pairing, part of the mobile  $C_I$  species will interact with remaining substitutional C atoms through, for instance, reaction (11). These C-related trapping reactions affect measurements of the interstitial diffusivity  $D_I$  in Si. Figure 24 compares typical values for  $D_I$  from metal diffusion studies<sup>15</sup> with results obtained from the present experiments using MBE-grown B superlattices (Sec. IV B). The values for  $D_I$  at 800 °C vary from  $10^{-6}$  to  $10^{-12}$   $\text{cm}^2/\text{s}$ , while the activation energies for diffusion range from  $\sim 1$  to  $\sim 3.5$  eV. Also, the diffusion range of interstitials in Si superlattices grown by chemical-vapor deposition has been shown to be much larger than in MBE-grown Si.<sup>27</sup> This discrepancy between the various experiments has been ascribed to the fact that the migration of self-interstitials is perturbed by the presence of interstitial traps in Si,<sup>18,19</sup> and presumably C is the dominant impurity as demonstrated above.

The presence of trapping sites ( $T$ ) will impose a local equilibrium between free ( $I$ ) and trapped interstitials ( $IT$ ) according to

$$[IT] = k_T [I] ([T] - [IT]). \quad (12)$$

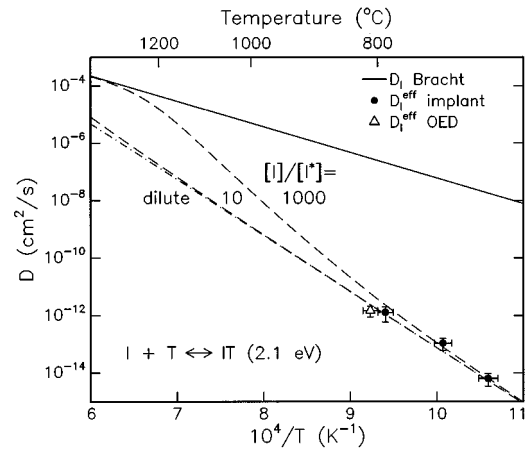


FIG. 24. Interstitial diffusivities in silicon. Solid lines refer to data derived from metal diffusion studies (Ref. 15), whereas points are from MBE marker layer experiments (Sec. IV and Ref. 35). The dashed lines refer to model fits of trap-limited diffusion assuming immobile traps, Eq. (13).

Constant  $k_T$  can be approximated by  $k_T \approx N_s^{-1} \exp(E_T/kT)$ , with  $E_T$  the energy difference between the free and bound states of  $I$ . For immobile traps, the interstitial diffusion flux  $J_I$  is entirely carried by the mobile species  $I$ , and the effective diffusivity  $D_I^{\text{eff}}$  for the total interstitial distribution  $[I] + [IT]$  is defined through

$$J_I = -D_I \nabla [I] \equiv -D_I^{\text{eff}} \nabla ([I] + [IT]).$$

For a uniform distribution of traps ( $\nabla [T] = 0$ ), the evaluation of this definition yields

$$D_I^{\text{eff}} = \frac{D_I}{1 + k_T [T] / \{1 + k_T [I]\}^2}. \quad (13)$$

Equation (13) was fitted to our TED and OED measurements of the interstitial diffusivity in Fig. 24 by taking  $D_I$  and  $[I^*]$  from the metal diffusion experiments of Ref. 15. Furthermore,  $[T]$  was fixed at  $10^{18}/\text{cm}^3$  to match the C content in our samples, and the average interstitial concentration in the TED and OED experiments was taken as  $1000 \times [I^*]$  and  $10 \times [I^*]$ ,<sup>28</sup> respectively. Using  $E_T = 2.1$  eV, the calculations for  $D_I^{\text{eff}}$  indeed reconcile the discrepancy between metal diffusion studies and our experimental data.

A severe limitation of the above analysis, however, is the simplifying assumption of immobile traps, whereas C–I pairing through reaction (10) leads to the formation of mobile  $C_I$  complexes. This implies that the interstitial flux  $J_I$  is actually carried by the migration of both  $I$  and  $C_I$ . In order to evaluate the effect of trapping reactions (10) and (11) on the diffusion of free interstitials, the full set of coupled diffusion and trapping equations was solved using the process simulator PROPHET.<sup>49,89</sup> The diffusivity of  $C_I$  was taken as  $D_{C_I} = 2.5 \times 10^{-3} \exp(-H_{C_I}^m/kT)$   $\text{cm}^2/\text{s}$ , with  $H_{C_I}^m = 0.8$  eV.<sup>81</sup> The trapping enthalpies for reactions (10) and (11) were assumed to be 1.7 and 0.9 eV, respectively, in accordance with recent first principle calculations.<sup>74</sup>

Figure 25 shows the evolution of the distributions of  $I$ ,  $C_I$ ,  $C_I C_s$ , and  $C_s$  at 800 °C. These profiles were calculated by assuming an interstitial injection level of  $1000 \times [I^*]$  at

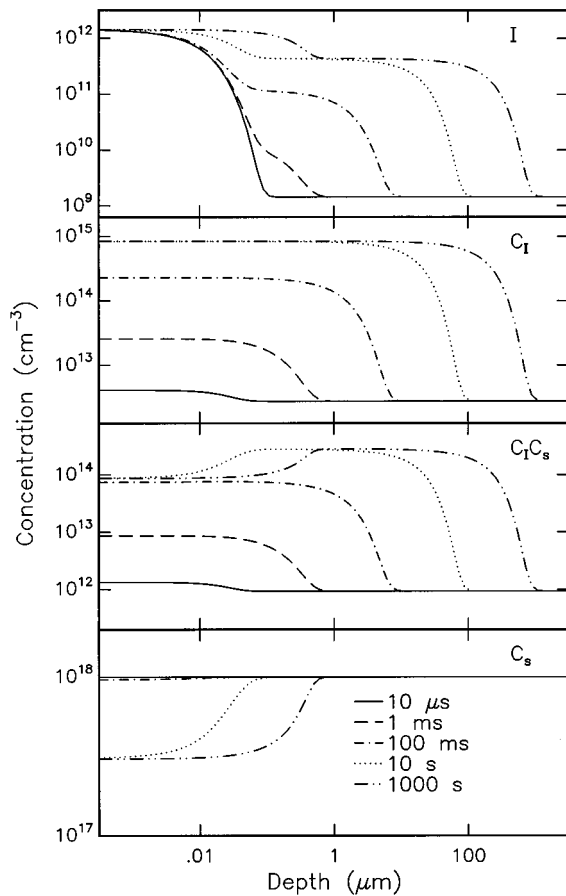


FIG. 25. Profiles of Si self-interstitials  $I$ , carbon-interstitial complexes  $C_I$ ,  $C_I C_s$  pairs, and substitutional C during diffusion at 800 °C, which were obtained by using the numerical calculations.

the surface, typical of TED. It is obvious that the simultaneous migration of  $I$  and  $C_I$  introduces a strong concentration dependence in the interstitial diffusion profile, which unfortunately obstructs the extraction of effective interstitial diffusivities for comparison with experimental data. Nevertheless, the important conclusion from Fig. 25 is that the apparent interstitial diffusivity in marker layer studies will depend critically on how the experimental conditions (e.g., interstitial injection levels and C content) modify the relative strength of  $I$  and  $C_I$  diffusion.

Carbon should also affect the analysis of metal diffusion studies. In an extensive number of experiments (e.g., Refs. 15 and 68), the diffusion profiles of various metals in Si (Au, Zn, and Pt) have been used to derive values for  $D_I$  and  $[I^*]$ . It was shown almost 20 years ago<sup>90</sup> that increasing the C concentration in Si accelerates the in-diffusion of interstitial Au ( $Au_i$ ), which was ascribed<sup>84</sup> to C trapping the interstitials formed in the kick-out reaction,



where  $Au_s$  denotes Au incorporated on substitutional sites. In most papers on metal diffusion, the C– $I$  interaction is fully ignored in spite of the fact that the C content in “standard” Si wafers could be as high as  $\sim 10^{17}/\text{cm}^3$ . Therefore, Zn diffusion data from Ref. 15 were reanalyzed by explicitly in-

cluding the trapping of interstitials at immobile, nonannihilating traps into our process simulator.<sup>89</sup> Independent of the trap concentration  $[T]$ , excellent fits to the measured diffusion profiles of Zn are obtained.<sup>89</sup> The extracted value for  $[I^*]$  varies inversely with  $[T]$ , while the product of  $[I^*]$  and  $D_I$  remains constant. This implies that metal diffusion experiments only provide direct information on the Si self-diffusion coefficient, that is,  $[I^*]D_I$ . The separate determination of  $[I^*]$  and  $D_I$ , on the other hand, requires detailed knowledge about the interaction of  $I$  with C or other impurities. Further experiments and analyses are required to solve this enigma.

## VII. PHYSICAL MODELING

### A. Monte Carlo simulations

The experiments in Secs. III and IV have shown that the rate and strength of interstitial injection during TED is controlled by the evaporation of  $\{311\}$  defects, that is, for the implantation regime presently explored. Implementation of this concept into process modeling tools requires a detailed understanding of the kinetics and parameters that are involved in the formation and annealing of implantation damage. For instance, it is *a priori* not clear how the as-implanted population of vacancies and interstitials develops into a distribution of rodlike interstitial clusters in the early stage of annealing. To help elucidate these processes, an atomistic process simulator was developed.<sup>63</sup> This simulator includes a Monte Carlo diffusion code coupled to the MARLOWE<sup>91</sup> computer code, which employs the binary collision approximation to estimate ion-induced defect formation in silicon. The parameters used in the Monte Carlo simulations were derived from molecular dynamics calculations using the Stillinger–Weber potential for Si.<sup>92</sup> More details about the new simulator have been given in a recent article by Jaraíz *et al.*<sup>63</sup>

The simulation of a typical room-temperature implant of  $5 \times 10^{13}/\text{cm}^2$ , 40 keV Si into Si(100) indicate that  $\sim 520$  Frenkel pairs are generated per implanted ion. Approximately 70 interstitials per ion survive room-temperature recombination of interstitials and vacancies during and after implantation, which is implicitly accounted for in the modeling. The resulting defect population consists of small interstitial and vacancy clusters, which are distributed according to the initial MARLOWE depth profile of interstitials and vacancies.

For a subsequent anneal at 815 °C, free vacancies are emitted from their clusters, while the more tightly bound interstitials remain immobile in their small clusters. The random walk of the vacancies annihilates most of the interstitials. Although the dominant annihilation process is bulk recombination, some vacancies reach the surface (assumed to be a perfect sink) and annihilate there, leaving an excess of interstitials. Figure 26 shows the cumulative number of vacancies  $V_{\text{surf}}$  and of interstitials  $I_{\text{surf}}$  annihilated at the surface, per implanted ion, as a function of simulation time. The emission from the vacancy clusters can be easily identified as an increase in  $V_{\text{surf}}$ , especially after  $10^{-3}$  s, when the larger clusters break up. At  $\sim 1$  s, all of the vacancies have disappeared with the overwhelmingly dominant mechanism being

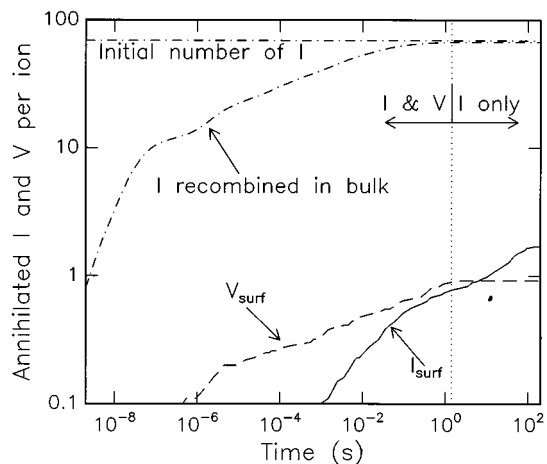


FIG. 26. Monte Carlo calculations of damage annealing in ion-implanted silicon (40 keV Si,  $5 \times 10^{13}/\text{cm}^2$ ). Comparison between the number of interstitials recombined with vacancies in the bulk and the number of vacancies  $V_{\text{surf}}$  and interstitials  $I_{\text{surf}}$  annihilated at the surface.

bulk recombination; only 1% of the vacancies diffuse to the surface.

Figure 27 plots the net excess of interstitials (interstitials minus vacancies), per implanted ion, throughout the anneal. The starting value (1.3) corresponds to the situation after the room-temperature implant, and includes the contribution of the implanted ion (the true +1), the sputtered Si atoms (-0.3), the trapping of vacancies at oxygen traps (+0.3), and the surface contribution (0.3) due to the fact that vacancies diffuse faster than interstitials and are on average slightly closer to the surface. The number of interstitials remaining when all the vacancies have disappeared is  $\sim 1$  per implanted ion, in agreement with the measurements in Fig. 7. It is quite remarkable that the full blown calculation, with the sputtering and surface terms, gives such a good approximation of the +1 model.

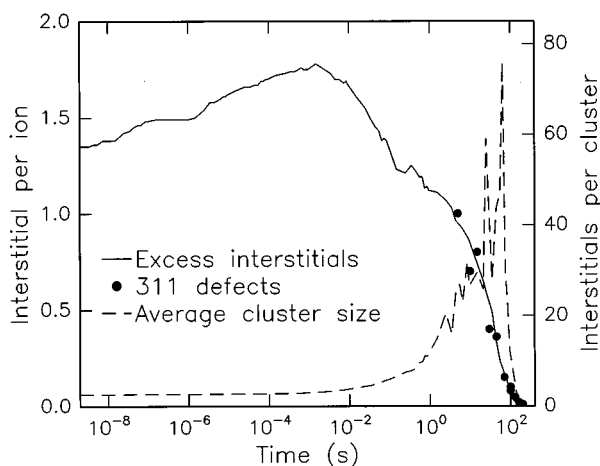


FIG. 27. Monte Carlo calculations of the net excess of interstitials per implanted ion during the 815 °C anneal. The solid points represent experimental data from TEM measurements of {311} defects (Fig. 5). Also shown is the average interstitials cluster size.

Upon continued annealing, small interstitial clusters undergo an Ostwald ripening process (Fig. 27, dashed line), analogous to the observed dynamics for {311} defects in Fig. 4. Eventually, the large clusters dissolve by emitting interstitials that subsequently annihilate at the front surface. The effect of trapping centers is almost negligible because of their low concentration relative to the interstitial concentration in the ion-implanted region. The dominant initial process during the high-temperature anneal is interstitial-vacancy recombination in the bulk of the material. Consequently, the imbalance in the interstitial and vacancy concentration arising from the implanted ion (the +1 model) dominates the excess interstitial concentration. This was confirmed by a simulation where the implanted ion was intentionally removed from the diffusion process. In that case the simulation yields +0.3 for the excess interstitial level, as opposed to +1.3. The clustering mechanism only establishes the time scale as was shown by an annealing simulation without clusters ( $E_{\text{bind}}=0$  for all clusters), in which case the vacancies disappear in  $5 \times 10^{-6}$  s, leaving +1.3 interstitials per implanted ion. The +1 model is, therefore, physically plausible because of the dominant role of bulk recombination, with only minor deviations due to sputtering and surface annihilation. This feature makes it a particularly robust approximation for process simulation tools, only weakly sensitive to changes in the implant or anneal parameters.

Finally, the implications of these results for TED can be assessed. A close correlation between the excess interstitials and the induced TED can be drawn from the free interstitial distribution, time-integrated throughout the anneal. It is found that most of the TED occurs after the vacancies have fully disappeared,<sup>63</sup> which explains why continuum simulators yield reasonable predictions using the +1 model in this damage regime. However, simulations for implant doses as low as  $5 \times 10^9/\text{cm}^2$  demonstrate that TED predominantly takes place before all vacancies have recombined. In this case, the probability of an interstitial interacting with a dopant atom has become greater than with a vacancy, because of the dilute interstitial and vacancy population.<sup>26,93</sup> This notion could explain the observation that the total broadening of B marker layers induced by TED declines with decreasing implantation dose, saturating at a fixed, nonequilibrium level for low doses.<sup>23</sup>

Although the +1 model seems to be appropriate for sufficiently high implantation doses ( $>5 \times 10^{12}/\text{cm}^2$ ), successful implementation of this model into process simulators requires detailed description of how interstitial clusters (i.e., {311} defects and dislocation loops) decay as a function of the implant (energy, dose) and annealing conditions (time, temperature). One example will be given in the following subsection. Modeling for lower doses should also include the fact that the average number of interstitial diffusion steps prior to recombination progressively increases with decreasing ion dose, leading to a more efficient damage-dopant coupling.

## B. Process simulations

The concept of interstitial clustering has been incorporated into the process simulator PROPHET.<sup>49,94</sup> The basis of



the model is that an interstitial in a cluster may spontaneously escape at a rate given by the interstitial hopping frequency and the binding energy to the cluster, while the clusters grow whenever diffusing interstitials are trapped by a cluster. The overall equation governing cluster kinetics is given by

$$\frac{d[I_{cl}]}{dt} = 4\pi\alpha a D_I [I][I_{cl}] - [I_{cl}] \frac{D_I}{a^2} \exp\left(-\frac{E_b}{kT}\right), \quad (15)$$

where  $D_I = D_0 \exp(-E_m/kT)$  is the interstitial diffusivity,  $a$  is the average interatomic spacing,  $\alpha$  is the capture radius expressed in units of  $a$ ,  $[I_{cl}(x,t)]$  is the concentration of interstitials trapped in clusters, and  $[I(x,t)]$  is the concentration of free interstitials. Whenever free interstitials are numerous, the first term dominates and  $[I_{cl}]$  grows exponentially until it is balanced by the evaporation flux. Equating the first and second terms in Eq. (15) yields the following expression for the interstitial concentration  $[I_e]$  in equilibrium with the defect clusters:

$$\frac{[I_e]}{[I^*]} = \frac{1}{4\pi\alpha\Gamma} \exp\left(\frac{E_f - E_b}{kT}\right), \quad (16)$$

where  $E_f$  is the formation energy of the interstitial and  $\Gamma$  is defined by the interstitial formation entropy through  $\Gamma = \exp(S_f/k)$ . As is obvious from the above equation, the interstitial supersaturation during TED is set by the balance between cluster evaporation and growth, provided that the initial interstitial level is high enough for stable clusters to be formed.

The evaporation rate of clusters after self-implantation can be estimated by assuming that the excess interstitial dose ( $Q \approx +1$ ) immediately condenses into clusters upon annealing. The loss of interstitials from the cluster region is controlled by the diffusive interstitial flux to the surface, which can be approximated by  $D_I [I_e]/R_p$ , where  $R_p$  is the projected ion range. Substituting the supersaturation of Eq. (16), the effective time needed to dissolve the clusters is given by Eq. (17). Thus, the evaporation time is thermally activated according to

$$\tau = \frac{4\pi\alpha R_p Q}{D_0 N_s} \exp\left(\frac{E_m + E_b}{kT}\right). \quad (17)$$

This model reproduces TEM observations that the  $\{311\}$  decay rate decreases with increasing ion dose and energy.<sup>60,64</sup> Applying this model to the  $5 \times 10^{13}/\text{cm}^2$ , 40 keV Si implants of Figs. 2–5, assuming  $\alpha=1$ , and using the most recent experimental values of  $D_I$  and  $[I^*]$ ,<sup>15</sup> yields  $\tau=42$  s at 815 °C and  $\tau=14\,600$  s at 670 °C, in perfect agreement with the experiments in Fig. 5. The activation energy  $E_b + E_m$  was taken to be 3.57 eV, in accordance with the TED time constants in Fig. 6 and in Ref. 11. A more exact calculation was carried out using the PROPHET simulator with the above numerical values to solve the differential equations for interstitial transport, recombination, and reaction with clusters in space and time. The result is shown in Fig. 28. The detailed calculation confirms the initial impression that the model captures the time and temperature dependence of  $\{311\}$  cluster evaporation. There is some discrepancy in the shape of the evaporation curves in that the simulated curves are more

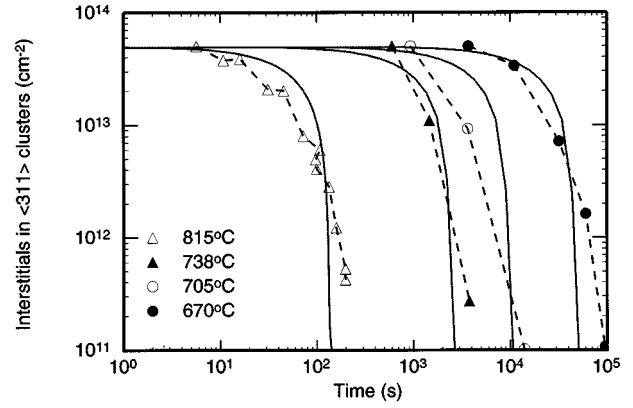


FIG. 28. Simulation of the number of interstitials contained in clusters, as a function of time, at various annealing temperatures. The experimental data are reproduced from Fig. 5. The simulation model predicts the time and temperature dependence of  $\{311\}$  evaporation.

abrupt than the experimental ones. Apart from the possibility of an experimental artifact (see Sec. III A), this dissimilarity is probably due to ignoring the dependence of the binding energy on cluster size. Including Ostwald ripening in a more sophisticated model with a distribution of cluster sizes would probably improve the evaporation behavior; yet, it is satisfying that this single population model already predicts the time to remove a given dose of interstitials with an error of only 30%.

Having established  $E_b + E_m = E_{\text{evap}} = 3.57$  eV, and knowing the interstitial self-diffusion energy  $E_f + E_m = E_{\text{SD}}$ , then the formation energy per atom of a  $\{311\}$  cluster is given by the difference  $E_{311} = E_{\text{SD}} - E_{\text{evap}} = E_f - E_b = 1.38$  eV (see Fig. 29). This is in very satisfactory agreement with recent predictions of  $E_{311}$  from molecular dynamics calculations ( $\sim 1.3$  eV),<sup>92</sup> and tight binding calculations (0.7–0.9 eV).<sup>95</sup> The formation energy per atom is also the activation energy of the interstitial supersaturation in Eq. (16), allowing the interstitial supersaturation during TED to be estimated as  $\sim 4000$  at 800 °C and  $\sim 400$  at 1000 °C. Typical experimental numbers are in the range of  $\sim 1000$ – $10\,000$  at 800 °C,<sup>7,10,11,96</sup> and 20–200 at 1000 °C.<sup>10,11</sup> The experimental values are generally underestimates since they attribute the diffusive motion

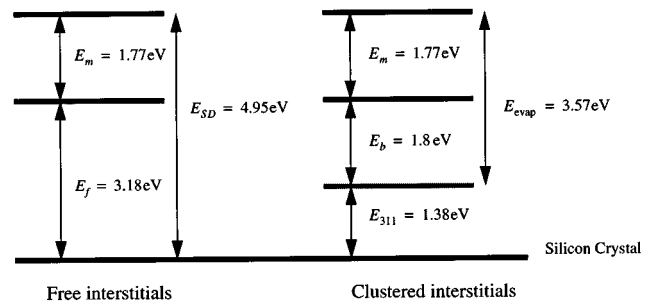


FIG. 29. The average energy of an interstitial in a  $\{311\}$  cluster is found to be 1.38 eV. This estimate is independent of the particular experimental values taken for  $D_I$  and  $[I^*]$ , as it comes out as the difference of the  $D_I/[I^*]$  product, which is in good agreement between various studies and the  $\{311\}$  evaporation time activation energies.

to the entire annealing time, whereas the transient vanishes some intermediate time during the anneal. From the interstitial profile in Fig. 12(b) it was derived that  $[I_e]/[I^*]$  is fixed at  $(7.7 \pm 3.8) \times 10^3$  during TED at 670 °C. This yields  $E_{311} = 1.3 \pm 0.1$  eV upon substitution in Eq. (16), in good agreement with the above numbers. It thus appears that the above model provides a self-consistent way of dealing with the clustering and injection of interstitials during TED, which can be efficiently implemented into process simulation programs.

A simple model of boron clustering can be developed on the following lines. One imagines a distribution of clusters, containing 2,3,4, etc., boron atoms. A cluster may shrink by spontaneously emitting a mobile boron-interstitial pair, or it may grow by capturing a free boron-interstitial pair. This yields rate equations which are analogous to those of Eq. (6a), but now with the addition of a decay term,

$$\frac{dN_3}{dt} = \frac{-N_3}{\tau} + 4\pi a_c D_{B_I} [B_I] N_2, \quad (18a)$$

$$\frac{dN_4}{dt} = \frac{-N_4}{\tau} + 4\pi a_c D_{B_I} [B_I] N_3, \quad \text{etc.}, \quad (18b)$$

where  $N_i$  is the number of clusters of size  $i$  and  $\tau$  is a spontaneous decay time. Multiplying each equation by  $i$  and summing over  $i$ ,

$$\frac{d}{dt} \left( \sum_i i N_i \right) = \frac{-\sum_i i N_i}{\tau} + 4\pi a_c D_{B_I} [B_I] \sum_i i N_i. \quad (19)$$

The rate equation for the total number of boron atoms in clusters,  $B_c = \sum_i i N_i$ , is then

$$\frac{d[B_c]}{dt} = -\frac{[B_c]}{\tau} + 4\pi a_c D_{B_I} [B_I] [B_c]. \quad (20)$$

This result relies on the approximations that  $\tau$  and  $a_c$  are independent of cluster size, and that the average cluster contains at least three or four boron atoms. Making one final assumption that the pairing reaction for forming  $B_I$  [Eq. (4a)] is in equilibrium,

$$\frac{d[B_c]}{dt} = -\frac{[B_c]}{\tau} + k_f [B_s] [I] [B_c], \quad (21)$$

with  $k_f$  a rate constant expressed in  $\text{cm}^6/\text{s}$ . The equation predicts that when the number of interstitials is large, the second term will dominate and lead to an exponential growth in  $[B_c]$ . The exponential growth will continue until the second term is reduced and the first term increased to bring them into balance. When this occurs,

$$\frac{1}{\tau k_f [I]} = [B_s]. \quad (22)$$

That is to say, the free boron concentration  $[B_s]$  will be lowered until it reaches a quasisolubility which is inversely related to the interstitial concentration  $[I]$ . This is consistent with the observation that the apparent solubility in each superlattice spike is inversely related to the amount of diffusion seen in that spike (see, for instance, Fig. 11).

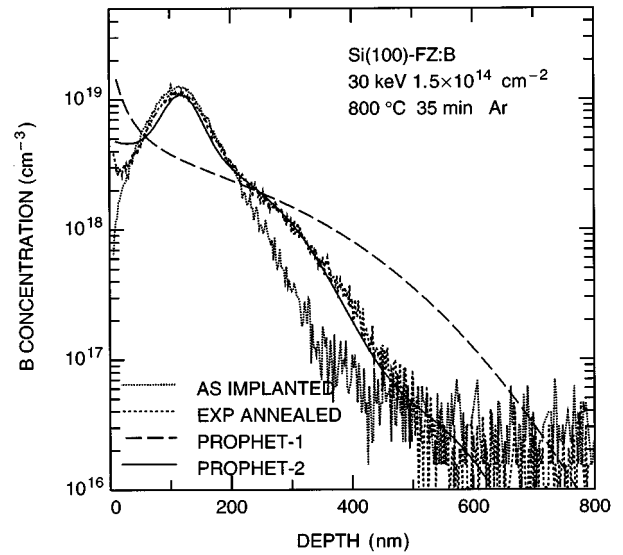


FIG. 30. PROPHET simulation of TED for the experiment of Fig. 1 ( $1.5 \times 10^{14}/\text{cm}^2$ , 30 keV  $^{10}\text{B}$  implant diffused at 800 °C for 35 min). A comparison is made between the default diffusion model (PROPHET-1) and the new model including interstitial and B clustering (PROPHET-2). This figure clearly illustrates the improvements that have been made.

The above approaches for dealing with interstitial and boron clustering were implemented into PROPHET and used to simulate the initial TED experiment of Fig. 1. It was required to take the net interstitial excess at +0.5 instead of +1.0 to match the diffusion in the tail of the profile. A similar effect has been seen in other work<sup>71</sup> where implanting B and Si at the same dose and energy gave identical TED in buried markers. Since the B is implanted more deeply, one would expect more TED than from the Si implant. That one does not is an indication that the net interstitial excess is smaller with B implants than Si implants. Alternatively, this discrepancy could reflect the trapping of some of the interstitials in B clusters (Fig. 8). As can be seen from Fig. 30, the fit to the B profile has greatly improved as a result of the physical insights presented in this article. Of course, more simulations are required to test the present model for a wider range of implant and annealing conditions.

## VIII. SUMMARY: THE LIFE OF THE INTERSTITIAL

This article has dealt with clustering and diffusion phenomena involving dopants and defects which are activated in ion-implanted silicon during annealing. The common microscopic agent of these processes is the Si self-interstitial, and the physical mechanisms which control transient enhanced dopant diffusion can be summarized in a qualitative manner by following the life of the interstitial.

Ion implantation leads to an athermal generation of interstitials and vacancies through the collisional displacements of lattice atoms. The average number of Frenkel pairs that is generated per incoming ion depends on the ion species and energy, and may vary from tens to thousands for keV implants of atoms such as B, Si, or P. The Monte Carlo simulations in Sec. VII A have shown that a fraction of the Frenkel pairs recombines during and after implantation at

room temperature, and the remaining interstitials and vacancies are contained in small clusters. Upon annealing, these clusters will dissolve by emitting point defects (interstitials and/or vacancies), which will eventually recombine with their free or clustered counterparts, annihilate at the surface, or diffuse into the bulk. It was demonstrated by TEM measurements in Sec. III that for sufficiently high damage levels ( $40 \text{ keV Si}$ ,  $>1 \times 10^{13}/\text{cm}^2$ ), the resulting excess number of interstitial atoms approximately equals the imbalance in the interstitial and vacancy concentrations resulting from the extra implanted atom (the +1 model). This suggests that  $I-V$  recombination is the dominant decay mechanism in the initial annealing stage, as reconfirmed by the Monte Carlo simulations in Sec. VII A.

The excess interstitials are contained in  $\{311\}$  defect clusters for doses in the range from  $5 \times 10^{12}$  to  $1 \times 10^{14}/\text{cm}^2$ , and these defects sustain a local supersaturation of interstitials by emitting and recapturing interstitials during continued annealing (Ostwald ripening). Interstitials are gradually lost from the damage region through diffusion into the bulk and to the surface, the latter most likely being the dominant loss mechanism.<sup>31</sup> The rate at which this decay occurs is determined by the average binding energy of interstitials at  $\{311\}$  ( $\sim 1.3 \text{ eV}$ ), the proximity of the surface, and the initial interstitial concentration as it is set by the implant dose. For sufficiently high doses ( $>1 \times 10^{14}/\text{cm}^2$ ) and annealing temperatures,  $\{311\}$  defects may unfault into more stable dislocation loops which will change the kinetics of interstitial injection.

Those interstitials which have escaped from the damage region into the bulk of the material may pair with dopants such as B and P, or with impurities such as C. The first interaction causes the local dopant-interstitial pair concentration to increase above the equilibrium level, thereby causing enhanced diffusion. For sufficiently high B levels, the wind of diffusing interstitials drives substitutional B into metastable clusters at concentrations below the solid solubility limit. This clustering process is most likely accompanied by the trapping of interstitials, which perturbs the interstitial flow.

The coupling of interstitials with C leads to the formation of highly mobile  $C_I$  pairs. This process reduces the amount of interstitials available for pairing with dopants, leading to a strong reduction in the enhanced diffusion and clustering of B for sufficiently high C concentrations ( $\sim 10^{19}/\text{cm}^3$ ). The rapidly migrating  $C_I$  pairs, which carry part of the net interstitial diffusion flux, can undergo further trapping reactions with ubiquitous impurities in Si such as substitutional C. The resulting retardation of the interstitial transport depends critically on the injected level of interstitials and on the concentrations of  $C_s$ , a notion which would explain the large variation in published interstitial diffusivities. Eventually, interstitials trapped in B- and C-related clusters will be reemitted and will continue to migrate through trapping and detrapping, until the equilibrium between free interstitials and vacancies is fully recovered.

Some caution is required with respect to the modeling of TED of ion-implanted B. When the high B concentration is contained inside the ion-damaged region, some fraction of

the interstitial-enhanced B diffusion and clustering may actually occur as the interstitial and vacancy population collapses. This would require a full-blown evaluation of the coupled defect-defect and defect-dopant interactions to assess the B profiles and the defect distribution before the  $\{311\}$ -controlled diffusion regime kicks in. This is just one question which remains to be answered among many others: By which microscopic mechanism does B diffuse? Can the various published diffusivities of Si indeed be reconciled on the basis of C-interstitial trapping reactions? How do  $\{311\}$  defects evolve into dislocation loops, and how does this process affect the interstitial injection kinetics? Do the interstitial and vacancy populations behave independently for high-energy implants? These and related issues will certainly provide a challenge to the silicon research community for many years to come.

## ACKNOWLEDGMENTS

A large number of people has contributed significantly to the present work in the form of discussions and technical support. Among them are J. L. Benton, T. Boone, G. S. Higashi, and F. C. Unterwald at Bell Laboratories, T. Diaz de la Rubia and J. Zhu at Lawrence Livermore National Laboratories, and N. E. B. Cowern at Philips Research Laboratories. A portion of this work was sponsored by the U.S. Department of Energy, Office of Energy Research, Laboratory Technology Applications Division and the Division of Materials Sciences under Contract No. DE-AC05-96OR22464 with Lockheed Martin Energy Research Corp.

- <sup>1</sup>W. K. Hofker, H. W. Werner, D. P. Oosthoek, and N. J. Koeman, *Appl. Phys.* **4**, 125 (1974).
- <sup>2</sup>R. T. Hodgson, V. R. Deline, S. Mader, and J. C. Gelpey, *Appl. Phys. Lett.* **44**, 589 (1984).
- <sup>3</sup>R. B. Fair, J. J. Wortman, and J. Liu, *J. Electrochem. Soc.* **131**, 2387 (1984).
- <sup>4</sup>K. Cho, M. Numan, T. G. Finstad, W. K. Chu, J. Liu, and J. J. Wortman, *Appl. Phys. Lett.* **47**, 1321 (1985).
- <sup>5</sup>N. E. B. Cowern, D. J. Godfrey, and D. E. Sykes, *Appl. Phys. Lett.* **49**, 1711 (1986).
- <sup>6</sup>A. E. Michel, W. Rausch, P. A. Ronsheim, and R. H. Kastl, *Appl. Phys. Lett.* **50**, 416 (1987); **51**, 487 (1987).
- <sup>7</sup>M. D. Giles, *J. Electrochem. Soc.* **138**, 1160 (1991).
- <sup>8</sup>Y. M. Kim, G. Q. Lo, D. L. Wong, A. F. Tasch, and S. Novak, *Appl. Phys. Lett.* **56**, 1254 (1990).
- <sup>9</sup>A. E. Michel, *Nucl. Instrum. Methods Phys. Res. B* **37/38**, 379 (1989).
- <sup>10</sup>N. E. B. Cowern, K. T. F. Janssen, and H. F. F. Jos, *J. Appl. Phys.* **68**, 6191 (1990).
- <sup>11</sup>S. Solmi, F. Baruffaldi, and R. Canteri, *J. Appl. Phys.* **69**, 2135 (1991).
- <sup>12</sup>P. M. Fahey, P. B. Griffin, and J. D. Plummer, *Rev. Mod. Phys.* **61**, 289 (1989).
- <sup>13</sup>M. Orlowski, C. Mazuré, and F. Lau, in *Tech. Digest IEDM*, 1987, p. 632.
- <sup>14</sup>C. S. Rafferty, H.-H. Vuong, S. A. Eshraghi, M. D. Giles, M. R. Pinto, and S. J. Hillenius, in *Tech. Digest IEDM*, 1993, p. 311.
- <sup>15</sup>H. Bracht, N. A. Stolwijk, and H. Mehrer, *Phys. Rev. B* **52**, 16 542 (1995).
- <sup>16</sup>R. F. Peart, *Phys. Status Solidi* **15**, K119 (1966); J. M. Fairfield and B. J. Masters, *J. Appl. Phys.* **38**, 3148 (1967); L. Kalinowski and R. Seguin, *Appl. Phys. Lett.* **35**, 211 (1979); **36**, 171 (1980); J. Hirvonen and A. Anttila, *ibid.* **35**, 703 (1979); F. J. Demond, S. Kalbitzer, H. Mannsperger, and H. Damjantschitsch, *Phys. Lett. A* **93**, 503 (1983).
- <sup>17</sup>N. A. Stolwijk, J. Hölzl, W. Frank, E. R. Weber, and H. Mehrer, *Appl. Phys. A* **39**, 37 (1986).
- <sup>18</sup>P. B. Griffin, S. T. Ahn, W. A. Tiller, and J. D. Plummer, *Appl. Phys. Lett.* **51**, 115 (1987).
- <sup>19</sup>N. E. B. Cowern, *Appl. Phys. Lett.* **64**, 2646 (1994).

- <sup>20</sup>R. B. Fair, *J. Electrochem. Soc.* **137**, 667 (1990).
- <sup>21</sup>H. U. Jäger, *J. Appl. Phys.* **78**, 176 (1995).
- <sup>22</sup>P. B. Griffin, P. M. Fahey, J. D. Plummer, and R. W. Dutton, *Appl. Phys. Lett.* **47**, 319 (1985).
- <sup>23</sup>P. A. Packan and J. D. Plummer, *Appl. Phys. Lett.* **56**, 1787 (1990).
- <sup>24</sup>N. E. B. Cowern, K. T. F. Janssen, G. F. A. van de Walle, and D. J. Gravesteijn, *Phys. Rev. Lett.* **65**, 2434 (1990).
- <sup>25</sup>N. E. B. Cowern, G. F. A. van de Walle, D. J. Gravesteijn, and C. J. Vriezema, *Phys. Rev. Lett.* **67**, 212 (1991).
- <sup>26</sup>N. E. B. Cowern, G. F. A. van de Walle, P. C. Zalm, and D. J. Oostra, *Phys. Rev. Lett.* **69**, 116 (1992).
- <sup>27</sup>K. J. van Oostrum, P. C. Zalm, W. B. de Boer, D. J. Gravesteijn, and J. W. F. Maes, *Appl. Phys. Lett.* **61**, 1513 (1992).
- <sup>28</sup>H.-J. Gossmann, C. S. Rafferty, H. S. Luftman, F. C. Unterwald, T. Boone, and J. M. Poate, *Appl. Phys. Lett.* **63**, 639 (1993).
- <sup>29</sup>P. B. Griffin, R. F. Lever, P. A. Packan, and J. D. Plummer, *Appl. Phys. Lett.* **64**, 1242 (1994).
- <sup>30</sup>M. J. van Dort, H. Lifka, P. C. Zalm, W. B. de Boer, P. H. Woerlee, J. W. Slotboom, and N. E. B. Cowern, *Appl. Phys. Lett.* **64**, 2130 (1994).
- <sup>31</sup>P. A. Stolk, H.-J. Gossmann, D. J. Eaglesham, D. C. Jacobson, J. M. Poate, and H. S. Luftman, *Appl. Phys. Lett.* **66**, 568 (1995).
- <sup>32</sup>P. A. Stolk, D. J. Eaglesham, H.-J. Gossmann, and J. M. Poate, *Appl. Phys. Lett.* **66**, 1370 (1995).
- <sup>33</sup>D. R. Lim, C. S. Rafferty, and F. P. Klemens, *Appl. Phys. Lett.* **67**, 2303 (1995).
- <sup>34</sup>H.-J. Gossmann, C. S. Rafferty, P. A. Stolk, D. J. Eaglesham, G. H. Gilmer, J. M. Poate, H.-H. Vuong, T. K. Mogi, and M. O. Thompson, *Mater. Res. Soc. Symp. Proc.* **389**, 3 (1995).
- <sup>35</sup>H.-J. Gossmann, T. K. Mogi, C. S. Rafferty, P. A. Stolk, D. J. Eaglesham, H. S. Luftman, F. C. Unterwald, T. Boone, M. O. Thompson, and J. M. Poate, *Semiconductor Silicon—1995, Proceedings of the Electrochemical Society*.
- <sup>36</sup>D. J. Eaglesham, P. A. Stolk, H.-J. Gossmann, and J. M. Poate, *Appl. Phys. Lett.* **65**, 2305 (1994).
- <sup>37</sup>M. C. Ozturk, J. J. Wortman, C. M. Osburn, A. Ajmera, G. A. Rozgonyi, E. Frey, W.-K. Chu, and C. Lee, *IEEE Trans. Electron Devices* **ED-35**, 659 (1988).
- <sup>38</sup>A. J. Walker, P. H. Woerlee, H. G. Pomp, and N. E. B. Cowern, *J. Appl. Phys.* **73**, 4048 (1993).
- <sup>39</sup>V. Raineri, R. J. Schreuterkamp, F. W. Saris, K. T. F. Janssen, and R. E. Kaim, *Appl. Phys. Lett.* **58**, 922 (1991).
- <sup>40</sup>K. Kylesbech Larsen, V. Privitera, S. Coffa, F. Priolo, C. Spinella, M. Saggio, and S. U. Campisano, *Nucl. Instrum. Methods B* **112**, 139 (1996).
- <sup>41</sup>S. Nishikawa, A. Tanaka, and T. Yamaji, *Appl. Phys. Lett.* **60**, 2270 (1992).
- <sup>42</sup>N. E. B. Cowern, A. Cacciato, J. S. Custer, F. W. Saris, and W. Vanderhorst, *Appl. Phys. Lett.* **68**, 1150 (1996).
- <sup>43</sup>H. Wong, N. W. Cheung, P. K. Chu, J. Liu, and J. W. Mayer, *Appl. Phys. Lett.* **52**, 1023 (1988).
- <sup>44</sup>J. R. Liefting, J. S. Custer, and F. W. Saris, *Mater. Res. Soc. Symp. Proc.* **235**, 179 (1992); *Mater. Sci. Eng. B* **25**, 60 (1994).
- <sup>45</sup>S. Isomae, T. Ishiba, T. Ando, and M. Tamura, *J. Appl. Phys.* **74**, 3815 (1993).
- <sup>46</sup>H.-J. Gossmann, F. C. Unterwald, and H. S. Luftman, *J. Appl. Phys.* **73**, 8237 (1993).
- <sup>47</sup>P. A. Stolk, H.-J. Gossmann, D. J. Eaglesham, and J. M. Poate, *Nucl. Instrum. Methods B* **96**, 187 (1995).
- <sup>48</sup>J. W. Strane, S. R. Lee, H. J. Stein, S. T. Picraux, J. K. Watanabe, and J. W. Mayer, *J. Appl. Phys.* **79**, 637 (1996).
- <sup>49</sup>M. R. Pinto, D. M. Boulton, C. S. Rafferty, R. K. Smith, W. M. Coughran, Jr., I. C. Kizilyalli, and M. J. Thoma, in *Tech. Digest IEDM*, 1992, p. 923.
- <sup>50</sup>It should be noted that vacuum annealing has been shown to affect the equilibrium population of point defects in silicon to some degree (Ref. 35). As has been argued in Ref. 35, however, this vacuum effect is not likely to affect the present nonequilibrium experiments to a large extent.
- <sup>51</sup>G. L. Olson and J. A. Roth, *Mater. Sci. Rep.* **3**, 1 (1988).
- <sup>52</sup>Extrinsic diffusion conditions were taken into account through the enhancement factor  $\beta$ . An estimate for  $\beta$  at 670 °C was obtained by comparing B diffusion in superlattices with maximum doping levels near and well above the intrinsic carrier concentration ( $\approx 7 \times 10^{17}/\text{cm}^3$  at 670 °C); see results in Fig. 14. Analyzing these intrinsic and extrinsic experiments only yielded a self-consistent set of  $\langle D_B^{\text{int}} \rangle$  values if  $\beta$  was restricted to  $0 < \beta < 0.5$ ;  $\beta = 0.2$  has been applied here. For  $T = 790$  °C,  $\beta$  has been taken equal to 3.
- <sup>53</sup>S. Takeda, M. Kohyama, and K. Ibe, *Philos. Mag. A* **70**, 287 (1994).
- <sup>54</sup>A. Bourret, *Am. Inst. Phys. Conf. Ser.* **87**, 39 (1987).
- <sup>55</sup>I. G. Salisbury and M. H. Loretto, *Philos. Mag. A* **39**, 317 (1979).
- <sup>56</sup>M. Seibt, J. Imschweiler, and H.-A. Hefner, in *Semiconductor Silicon—1994, Proceedings of the Electrochemical Society, San Francisco*, p. 720.
- <sup>57</sup>311, “Applied Science” on *Grassroots* (Capricorn Records, Nashville, 1994).
- <sup>58</sup>It is assumed that the defects have a fixed width of 40 Å, and that the areal interstitial density in {311} defects is  $5 \times 10^{14}/\text{cm}^2$ .
- <sup>59</sup>D. J. Eaglesham, P. A. Stolk, J.-Y. Cheng, H.-J. Gossmann, T. E. Haynes, and J. M. Poate, *Inst. Phys. Conf. Ser.* **146**, 451 (1996).
- <sup>60</sup>K. S. Jones, J. Liu, L. Zhang, V. Krishnamoorthy, and R. T. DeHoff, *Nucl. Instrum. Methods B* **106**, 227 (1995).
- <sup>61</sup>K. S. Jones and D. Venables, *J. Appl. Phys.* **69**, 2931 (1991).
- <sup>62</sup>J. K. Listebarger, K. S. Jones, and J. A. Slinkman, *J. Appl. Phys.* **73**, 4815 (1993).
- <sup>63</sup>M. Jaraíz, G. H. Gilmer, J. M. Poate, and T. D. de la Rubia, *Appl. Phys. Lett.* **68**, 409 (1996).
- <sup>64</sup>D. J. Eaglesham, P. A. Stolk, H.-J. Gossmann, T. E. Haynes, and J. M. Poate, *Nucl. Instrum. Methods B* **106**, 191 (1995).
- <sup>65</sup>P. A. Stolk and H.-J. Gossmann (unpublished).
- <sup>66</sup>The effective depth of the source from the sample surface is assumed to be equal to the projected ion range for 40 keV Si of 600 Å.
- <sup>67</sup>H.-J. Gossmann, P. Asoka-Kumar, T. C. Leung, B. Nielsen, K. G. Lynn, F. C. Unterwald, and L. C. Feldman, *Appl. Phys. Lett.* **61**, 540 (1992).
- <sup>68</sup>F. F. Morehead, *Mater. Res. Soc. Symp. Proc.* **104**, 99 (1988).
- <sup>69</sup>T. E. Haynes, D. J. Eaglesham, P. A. Stolk, H.-J. Gossmann, D. C. Jacobson, and J. M. Poate, *Appl. Phys. Lett.* **69**, 1376 (1996).
- <sup>70</sup>L. C. Kimerling, M. T. Asom, J. L. Benton, P. J. Drevinsky, and C. E. Cafer, *Mater. Sci. Forum* **38-41**, 141 (1989).
- <sup>71</sup>P. B. Griffin, R. F. Lever, R. Y. S. Huang, H. W. Kennel, P. A. Packan, and J. D. Plummer, in *Tech. Digest IEDM*, 1993, p. 295.
- <sup>72</sup>D. Mathiot and J. C. Pfister, *J. Appl. Phys.* **55**, 3518 (1984).
- <sup>73</sup>M. Hane and H. Matsumoto, in *Tech. Digest IEDM*, 1991, p. 701; *IEEE Trans. Electron Devices* **ED-40**, 1215 (1993).
- <sup>74</sup>J. Zhu, T. Diaz de la Rubia, L. H. Yang, C. Mailhot, and G. H. Gilmer, *Phys. Rev. B* **54** 4741 (1996).
- <sup>75</sup>J. Vanhellemont and A. Romano-Rodríguez, *Phys. Status Solidi* **138**, 417 (1993).
- <sup>76</sup>L. H. Zhang, K. S. Jones, P. H. Chi, and D. S. Simons, *Appl. Phys. Lett.* **67**, 2025 (1995).
- <sup>77</sup>H. G. A. Huizing, C. C. G. de Visser, N. E. B. Cowern, P. A. Stolk, and R. C. M. de Kruif, *Appl. Phys. Lett.* **69**, 1211 (1996).
- <sup>78</sup>J. R. Liefting, R. C. M. Wijburg, J. S. Custer, H. Wallinga, and F. W. Saris, *IEEE Trans. Electron Devices* **ED-41**, 50 (1994).
- <sup>79</sup>I. Ban, M. C. Öztürk, K. Christensen, and D. M. Maher, *Appl. Phys. Lett.* **68**, 499 (1996).
- <sup>80</sup>A. R. Bean and R. C. Newman, *Solid State Commun.* **8**, 175 (1970).
- <sup>81</sup>G. D. Watkins and K. L. Brower, *Phys. Rev. Lett.* **36**, 1329 (1976); L. W. Song and G. D. Watkins, *Phys. Rev. B* **42**, 5759 (1990).
- <sup>82</sup>L. W. Song, X. D. Zhan, B. W. Benson, and G. D. Watkins, *Phys. Rev. B* **42**, 5765 (1990).
- <sup>83</sup>G. Davies, K. T. Kun, and T. Reade, *Phys. Rev. B* **44**, 12 146 (1991).
- <sup>84</sup>U. Gösele, *Mater. Res. Soc. Symp. Proc.* **59**, 419 (1986).
- <sup>85</sup>S. Pizzini, S. Binetti, M. Acciarri, and S. Acerboni, *Phys. Status Solidi A* **138**, 451 (1993).
- <sup>86</sup>A. Borghesi, *J. Appl. Phys.* **77**, 4169 (1995).
- <sup>87</sup>W. Skorupa and R. A. Yankov, *Mater. Chem. Phys.* **44**, 101 (1996).
- <sup>88</sup>L. A. Ladd, J. P. Kalejs, and U. Gösele, *Mater. Res. Soc. Symp. Proc.* **36**, 89 (1985).
- <sup>89</sup>H.-J. Gossmann, P. A. Stolk, D. J. Eaglesham, C. S. Rafferty, and J. M. Poate, *Appl. Phys. Lett.* **67**, 3135 (1995).
- <sup>90</sup>M. J. Hill and P. M. Van Iseghem, in *Semiconductor Silicon—1977*, edited by H. R. Huff and E. Sirtl (The Electrochemical Society, Princeton, 1977), p. 521.
- <sup>91</sup>M. T. Robinson and I. M. Torrens, *Phys. Rev. B* **9**, 5008 (1974).
- <sup>92</sup>G. H. Gilmer, T. Diaz de la Rubia, D. M. Stock, and M. Jaraíz, *Nucl. Instrum. Methods Phys. Res. B* **102**, 247 (1995).
- <sup>93</sup>N. E. B. Cowern, G. F. A. van de Walle, P. C. Zalm, and D. W. E. Vandenhout, *Appl. Phys. Lett.* **65**, 2981 (1994).
- <sup>94</sup>C. S. Rafferty, G. H. Gilmer, M. Jaraíz, D. J. Eaglesham, and H.-J. Gossmann, *Appl. Phys. Lett.* **68**, 2395 (1996).
- <sup>95</sup>M. Kohyama and S. Takeda, *Phys. Rev. B* **51**, 13 111 (1995).
- <sup>96</sup>H. Park and M. E. Law, *Appl. Phys. Lett.* **58**, 732 (1991).